Spin-crossover nanoparticles anchored on MoS₂ layers for heterostructures with tunable strain driven by thermal or light-induced spin switching

Ramón Torres-Cavanillas, Marc Morant-Giner, Garin Escorcia-Ariza, Julien Dugay, Josep Canet-Ferrer, Sergio Tatay, Salvador Cardona-Serra, Mónica Giménez-Marqués, Marta Galbiati, Alicia Forment-Aliaga* and Eugenio Coronado*

Instituto de Ciencia Molecular (ICMol), Universidad de Valencia, C/ Catedrático José Beltrán 2, Paterna, 46980, Spain.
E-mail: alicia.forment@uv.es and eugenio.coronado@uv.es

In the last few years, the effect of strain on the optical and electronic properties of MoS₂ layers has been deeply studied. Complex devices have been designed where strain is externally applied on the 2D material. However, so far, the preparation of a reversible self-strainable system based on MoS₂ layers has remained elusive. In this work, spin-crossover nanoparticles are covalently grafted onto functionalized layers of semiconducting MoS₂ to form a hybrid heterostructure. We use the ability of spin-crossover molecules to switch between two spin states upon the application of external stimuli to generate strain over the MoS₂ layer. This spin crossover is accompanied by a volume change and induces strain and a substantial and reversible change of the electrical and optical properties of the heterostructure. This strategy opens the way towards a next generation of hybrid multifunctional materials and devices of direct application in highly topical fields like electronics, spintronics or molecular sensing.

The research on graphene and other two-dimensional (2D) materials has been propelled by the possibility of studying and exploiting the properties of matter in the 2D limit.[1] Nowadays, this topic is moving towards the assembly of monolayers of different types to afford van der Waals heterostructures.[2-4] In the 2D area, apart from the chemical functionalization of 2D materials,[5] the use of molecules as precursors, constituents or functional components of novel 2D systems

and heterostructures, has been scarcely investigated.[6,7] An interesting possibility in this context deals with the fabrication of mixed molecular/2D heterostructures, in which the properties of the "all surface" 2D layer can be tuned by the hybrid interface, i.e., by the interactions established between the molecules and the 2D material.[8-10]

A versatile family of 2D layered materials in which this molecular/2D concept can be exploited, is that formed by transition metal dichalcogenides (TMDCs)[11-13] of formula MX_2 (M = metals traditionally restricted to groups IV–VII; X = S, Se, Te). The members of this family display a wide range of electronic properties as a function of their composition and structures, including insulating, semiconducting, metallic and superconducting properties. Among them, the most deeply studied system is MoS_2, owing to its chemical stability and electronic properties. The weak interaction between stacked layers makes it feasible to isolate monolayers of this material, create van der Waals heterostructures and exploit them to design hybrid structures and electronic devices displaying new low-dimensional physics and unique functionalities.[14] Of special interest is the correlation between the electronic structure and the structural arrangement of S atoms in the monolayer. In fact, by a slight gliding of the S atoms, a switching between a trigonal prismatic symmetry around the Mo atom (2H-phase) and an octahedral one (1T-phase) occurs, giving rise to an electronic modulation of the 2D material from semiconducting to metallic.[15] This phase transition from 2H to 1T can be induced by different external stimuli such as chemical modification[16,17] or electron beam radiation,[18] while the inverse process can be achieved by thermal treatment,[19] infrared radiation,[20] or aging of the material.[21] An attractive possibility in this context is to induce the phase transition by applying strain. This has been theoretically predicted[22,23] and experimentally demonstrated in ultrathin MoS_2 layers in which a band gap narrowing under low tensile strain has been achieved, which enables the reversible tuning of their optical and electronic properties.[24,25] Sophisticated devices have been reported to prove the strain modulation of both the optical and electronic band gaps, through photoluminescence (PL), Raman spectroscopy,[26-28] and transport measurements.[28,29] In addition, an intrinsic negative piezoresistivity has been observed[25] and exploited to develop a piezoresistive composite in which the resistance decreases when the strain increases (negative Gauge factor).[30]

In this scenario, we have envisioned the possibility of preparing MoS_2-based heterostructures where the second component is an active molecular system that can directly and reversibly tune the strain applied on the 2D material and, therefore, its electronic structure and electric conductivity. We have chosen switchable molecular-based spin-crossover (SCO) materials for

this purpose. These materials are, in most cases, Fe(II) compounds that undergo a spin transition between low spin (LS with S=0) and high spin (HS with S=2) configurations upon the application of an external stimulus such as light, temperature, pressure or chemical activation. The LS to HS spin transition goes with a reversible ~ 0.2 Å lengthening of the Fe-Ligand coordination bonds distance.[31,32] Therefore, volume changes (up to 11.5%)[33] together with variations in the mechanical,[34] magnetic,[35] electrical[36] and optical properties[37] are expected depending on the spin state (See Supplementary Information, Movie 1). Interesting devices[38] and composites based on SCO materials embedded in different polymers have been already reported where a change in volume upon spin transition induces strain effects on a second component modifying their electrical and/or mechanical properties.[39-41]

However, in the field of 2D materials, the inducement of reversible strain by phase transition materials has not been demonstrated. In fact, all the examples of SCO/2D heterostructures reported so far are based on graphene. In these examples, a change in the electrical properties upon the spin transition has been observed, which has been mainly ascribed to electronic effects rather than mechanical ones. Thus, in the first reported example of SCO/2D device, based on the deposition of SCO nanoparticles on graphene,[42] model calculations showed that the change in the charge carrier mobility of the graphene was mainly due to its coupling with the phonon modes of the SCO nanoparticles, which differs depending on the spin state. Since this coupling is dependent on the dielectric permittivity of the SCO layer, a drop in the coupling is anticipated upon the spin transition due to the lower dielectric permittivity of the HS state. An electronic origin was also invoked in a heterostructure consisting in the deposition of a graphene layer on a large SCO crystal with a polymeric spacer in between. In this case, the mechanical influence of the SCO crystal over the properties of the 2D layer was minimized by the presence of the spacer. The small modification observed in the graphene conductivity was attributed to changes in the induced electrostatic potential caused by the change in the electric dipole moment of the SCO molecules in the two spin states.[43] Just very recently, the last example of SCO/graphene heterostructure has been reported, in which SCO molecules are sublimated on graphene.[44] Again a change in the electrical properties is observed that is ascribed to electronic changes upon the spin transition.

In the present work, we focus on SCO nanoparticles as phase transition material to induce a strain on the 2D material and thus modulate its electrical and optical properties. These nanoparticles are based on the [Fe(Htrz)$_2$(trz)](BF$_4$) coordination polymer (Htrz = 1,2,4-triazole and trz = triazolate) covered with a silica shell (from now on SCO-NPs).[45,46] The choice of these core-shell nanoparticles is based on the following considerations: (i) they have shown to

undergo a cooperative spin transition near room temperature, which is accompanied by a volume change and, depending on the purpose, their sizes and composition can be chemically tuned;[47,48] and (ii) the silica shell not only preserves the chemical stability of the SCO system without affecting the spin transition, Supplementary Information Fig. 10, but also provides an anchoring point for their further chemical functionalization, giving rise to robust heterostructures.[45]

Therefore, this work takes advantage of the previous broad physical knowledge of strain effects on MoS_2 to chemically design a SCO-NPs/MoS_2 hybrid heterostructure, which respond to external stimuli (temperature and light). In this smart heterostructure, strain effects are expected to be maximized thanks to the strong (covalent) anchoring of the nanoparticles on the MoS_2 surface.

Results

Chemical design of a hybrid SCO/MoS_2 heterostructure. In order to prepare the hybrid SCO/MoS_2 heterostructures, a straightforward solution grafting protocol that coats MoS_2 flakes with pre-synthesized SCO-NPs has been developed. This involves the chemical functionalization with 3-iodopropyl(trimethoxysilane) (IPTS) of ultrathin chemically exfoliated MoS_2 layers (CE-MoS_2), followed by the anchoring of the SCO-NPs to these functionalized layers via a covalent bond between the trimethoxysilane group and the silica shell[45,49] (Fig. 1). In more detail, this protocol starts with the preparation of CE-MoS_2 layers by reacting bulk 2H-MoS_2 with n-butyllithium (n-BuLi) used as reducing species.[50] During this process an electron transfer to MoS_2 occurs, giving rise to a partial structural reorientation and an electronic band structure modification, that triggers the transition from the semiconducting 2H to the metallic 1T-phase,[15,51] as confirmed by X-ray photoelectron (XPS) and Raman spectroscopies (Fig. 2 and Supplementary Information Tables 2, 3). After re-dispersion, the CE-MoS_2 flakes retain an excess of negative charge on their surfaces (Supplementary Information Fig. 1),[52] providing high colloidal stability and facilitating their ulterior covalent functionalization. On the other hand, core-shell SCO-NPs are synthesized following the protocol reported by some of us[48] (see Methods).

In order to functionalize the MoS_2 layers, a CE-MoS_2 suspension is mixed with a 3-iodopropyl(trimethoxysilane) (IPTS) solution. The excess of negative charge accumulated in CE-MoS_2 facilitates the nucleophilic attack to IPTS, resulting in the displacement of I and the formation of new covalent S-C bonds.[53] This gives rise to MoS_2 flakes decorated with propyltrimethoxysilane groups (PTS-MoS_2) (Fig. 1, step i). The successful anchoring of the

IPTS onto the MoS$_2$ surface is evidenced by a clear decrease in the measured ζ-potential value (from -32 mV to -6 mV, Supplementary Information Fig. 1).[53] The functionalization is confirmed by thermogravimetric analysis (TGA) and XPS. Through TGA a ~30% of functionalization is estimated (Supplementary Information Fig. 2), while the XPS confirms that functionalization takes place without modification of Mo and S oxidation states (Fig. 2a and b). However, during the process, CE-MoS$_2$ S$2p$, and Mo$3d$ peaks blue shift ~1 eV (Supplementary Information Table 3), suggesting a phase transition from the metallic 1T into the semiconducting 2H-phase. This conversion is confirmed in PTS-MoS$_2$ Raman spectrum where J peaks at 152, 232 and 326 cm^{-1} (fingerprint of the metallic phase),[54] decrease substantially at the expense of E$^1_{2g}$ and A$_{1g}$ peaks (Fig. 2c). Moreover, PL signal is restored, further supporting the conversion to the semiconducting phase[19,54] (Fig. 2d).

These results contrast with those reported by Chhowalla and coworkers where 1T-phase was preserved after functionalization but with unusual semiconducting properties and intense photoluminescence recovery.[53] Still, our results are in agreement with other publications where total[55] or partial[56] 1T to 2H phase transitions have been reported. These differences may be related to the synthetic protocols or the target molecule used for functionalization. As far as the synthetic protocol is concerned, we have investigated MoS$_2$ functionalized with iodoacetic acid, which has been prepared by following both, the protocol reported in reference[53] (involving longer reaction times in pure water) and our protocol (shorter reaction times in a mixture of solvents to minimize silane polymerization). We observe that the synthetic methodology plays a minor role. Thus, XPS spectra show that independent of the functionalization protocol, 1T-MoS$_2$ phase is not modified for this molecule, in contrast to what happens for the molecule used in the present work (IPTS), Supplementary Information Fig. 7 and tables 2-5. As far as the target molecule is concerned, we have seen significant differences in ζ-potential values of functionalized MoS$_2$ when different molecules are used. Thus, for the molecule used in reference[53] (2-iodoacetamide), as well as for the iodoacetic acid, the ζ-potential values are lower than that observed for PTS-MoS$_2$ (-20 meV compared to -6 meV) pointing out to a more efficient electron withdrawal from the IPTS, which could play a key role in MoS$_2$ phase stabilization.

Spectroscopic studies are indicative of the formation of a covalent bond between the MoS$_2$ and the IPTS. C-S vibration is expected at ~690 cm^{-1} in the FTIR spectra. Although a signal is observed in this region, unfortunately, it overlaps with ethanol and IPTS vibrations, hindering a definitive assignation of this peak. Nevertheless, the appearance of an additional contribution

at ~164 eV in the XPS S$2p$ signal that modifies the deconvolution analysis, points out to functionalization of sulphur.[53] An additional support for this covalent functionalization comes from energy-dispersive X-ray spectroscopy (EDAX) analysis performed on the thinnest flakes by a transmission electron microscope (TEM). These results show the presence of silicon and the absence of iodine, while confirming that the integrity of the flakes is maintained after functionalization (Supplementary Information Fig. 3).

In order to anchor the SCO-NPs to the functionalized layers forming the final heterostructure (SCO/MoS$_2$), the methoxysilane groups decorating PTS-MoS$_2$ are used to graft the SCO-NPs silica shell by mixing both suspensions[45,49] (Fig. 1, step ii). In this way, we obtain MoS$_2$ functionalized with SCO-NPs bearing two aspect ratios (70 x 40 nm and ~4 nm silica shell or 40 x 40 nm and ~3 nm shell, Supplementary Information Fig. 4,[48] SCO/MoS$_2$-1 and SCO/MoS$_2$-2a respectively) and three coverage degrees, accounted by the Fe:Mo ratios (See Methods). The coexistence of the two components in the heterostructure is confirmed by TEM, EDAX (Fig. 3 and Supplementary Information 5-6) and XPS (Supplementary Information Fig. 8), which exhibit the characteristic Fe$2p_{3/2}$ and Fe$2p_{1/2}$ peaks at ~709 eV and ~722 eV, respectively, coming from the SCO-NPs and similar Mo and S spectra to those recorded for PTS-MoS$_2$ (Fig. 2a, b). The integrity of the SCO-NPs in the hybrid is demonstrated by the magnetic data, which show a SCO thermal hysteresis very similar to the bulk, with transition temperatures at ~380 K ($T_{1/2}{}^{up}$) and ~340 K ($T_{1/2}{}^{down}$), Extended Data Fig. 1. Finally, XPS spectra repeated after keeping the sample one year in ambient conditions only shows a slight oxidation of the 2D layer, supporting a considerable robustness of SCO/MoS$_2$ to aging, Supplementary Information Fig. 9.

Influence of the SCO-NPs on the properties of MoS$_2$ in the hybrid SCO/MoS$_2$ heterostructure. To study the potential of SCO-NPs to modify the electronic structure of MoS$_2$ layers, we rely on electrical transport and PL measurements. In most of the SCO/MoS$_2$ samples, we observe thermal hysteresis in the conductivities (Fig. 4 and Supplementary Information Fig. 12) that follow well the SCO transitions observed from SQUID measurements (Extended Data Fig. 1). This electrical hysteresis is observed as two sharp changes in the conductance taking place exactly at the spin transition temperatures, suggesting that the changes observed in the electronic properties of the MoS$_2$ flakes are directly related to the spin transition of the SCO-NPs. The nanoparticles volume change induced by the spin transition, is expected to strain the flakes, resulting in an intrinsic modulation of the band gap structure of the layers, and thus modifying their conductivity.[28,29]

The strongest effects are obtained for heterostructures formed with SCO-NPs of 70 nm, named SCO/MoS$_2$-1. As reported in Fig. 4a, this sample shows a sharp increase of ca.900% in the conductance upon heating, coincident with the spin transition from LS to HS ($T_{1/2}{}^{up} \approx 370$ K), and a sharp drop in conductance during the reversal cooling down process, corresponding to the transition from HS to LS ($T_{1/2}{}^{down} \approx 340$ K) (Fig. 4a). Remarkably, this behaviour is opposite to the one observed in the SCO-NPs (Fig. 4b), where the nanoparticles are less conductive in the LS state than in the HS.[57,58] The reason is the following: while in pure SCO-NPs the conductivity occurs through the nanoparticles, in hybrid SCO/MoS$_2$ heterostructures the conductivity predominantly occurs through the semiconducting MoS$_2$ layers, which are at least 4 orders of magnitude more conductive than that of the SCO-NPs (Supplementary Information Fig. 12). In these heterostructures, the conductivity is higher for the HS because of the tensile strain generated on the MoS$_2$ when the spin transition occurs. For further details and discussion, see S.I. pages 14-19).[30]

Moreover, the above mentioned higher conductivity in SCO/MoS$_2$ samples shows that the typical insulator character of the SCO compounds is overcome. This feature is also very important when dealing with the sample stability. In fact, a general problem encountered when measuring the transport in pure SCO-NPs is the high voltages required (100 V), leading to a fast sample degradation.[59,60] On the contrary, the higher conductivities of the heteroestructures allow to measure at much lower voltages, thus guaranteeing sample integrity and the switching properties over several thermal cycles. Noticeably, the sample response was maintained unaltered over different days of temperature cycling. A total of about 20 temperature cycles have been performed on the sample and no relevant changes in the measured hysteresis were observed, Supplementary Information Fig. 11.

For the electronic characterization, SCO/MoS$_2$ samples decorated with SCO-NPs of different sizes were studied. Keeping the Fe:Mo ratio equal to 2 but using smaller SCO-NPs of 40 nm (SCO/MoS$_2$-2a), the observed thermal variation in the electrical response is qualitatively similar, but with a smaller switch of ca.30% (Supplementary Information Fig. 12). This result points out that, when the relative quantity of SCO-compound:MoS$_2$ is maintained, there is a more relevant effect induced on the 2D material by the size and shape of the nanoparticles (whose axial elongation increases as their size does), than by their number.

Additionally, we investigated the influence of the SCO-NPs/MoS$_2$ ratio on the transport properties, while keeping the shape and size of the particles unmodified. When the Fe:Mo ratio is further decreased from 2 to 0.4, SCO/MoS$_2$-2b, sample conductivity increases but the hysteretic effects coming from the SCO-NPs are completely lost, likely due to the low concentration of nanoparticles, Supplementary Information Fig. 12. Accordingly, sample conductivity decreases when the Fe:Mo ratio increases, and starting from a ratio of 5 (SCO/MoS$_2$-2c) sample behavior is reversed and approaches the one observed in assemblies of pure SCO-NPs, where the LS state becomes more conductive than the HS state[57,58] (Supplementary Information Fig. 12). From this reversal electrical behaviour, we can conclude that for high concentrations of SCO-NPs (Surface coverage ~100%, Supplementary Information Table 1), the charge transport is dominated by the nanoparticles. In contrast, when the concentration of the nanoparticles is decreased considerably (Surface coverage <60%, Supplementary Information Table 1), the transport mainly occurs through the MoS$_2$ flakes, without feeling SCO-NPs changes.

Noticeably, the decoration with bigger SCO-NPs (> 200-400 nm) was also achieved. Nevertheless, due to the tremendous strain caused by the spin transition, the compressed pellets fracture, making impossible its electrical characterization.

At this point, it may be of interest to compare the change in the electrical properties of SCO/MoS$_2$ with those observed for SCO/graphene heterostructures. As pointed out before, in graphene heterostructures, this change was predominantly electronic in nature. In contrast, in the SCO/MoS$_2$ heterostructure, this change is predominantly attributed to a mechanical modulation. The main reasons are the following: (i) the SCO/MoS$_2$ heterostructure has been chemically designed to maximize the mechanical coupling between the two components, thanks to the chemical functionalization of the layers, while minimizing the electronic coupling, thanks to the shieling provided by the SiO$_2$ layer and the PTS bridging molecules; and (ii) the 2H-MoS$_2$ layer behaves like a direct semiconductor, which, in contrast to graphene, has an optical band gap width very sensitive to strain.[61] In our case, this dominant strain effect is unambiguously proved by photoluminescence experiments (see below).

The PL properties of these heterostructures are shown in Fig. 5 and Extended Data Fig. 2-3. Because of the direct gap semiconductor nature of the MoS$_2$ monolayers (2H-phase), it is possible to gain direct information on their band gap energy through these measurements. [62,63] In fact, it is well known that when a tensile strain is applied to a MoS$_2$ layer, its PL redshifts and weakens its intensity as consequence of a narrowing in the band gap and a transition in the semiconductor from direct to indirect band gap behaviour occurs.[24,64] This is exactly the effect

we have observed by Raman spectroscopy performed in the SCO/MoS$_2$-1 and 2a hybrids in the two spin states (Fig. 5a, and Extended Data Fig. 3). Focusing on the hybrid made with larger nanoparticles, SCO/MoS$_2$-1, when the SCO-NPs are in the LS state (room temperature), a maximum in the PL signal (A peak) is observed at ~1.88 eV, which redshifts ~40 meV and decreases in intensity when the spin transition occurs (T > ~370). This variation can be monitored by measuring PL as a function of temperature. Complete cycles of heating and cooling are shown in Fig. 5b. We observe that the A peak intensity and energy differ at each temperature, showing a clear hysteretic behaviour (Extended Data Fig. 2), which completely resembles that of the spin state of the SCO-NPs, characterized by magnetic measurements and Raman spectroscopy (Extended Data Fig. 1 and 4).[31,65] This points out the clear effect of the nanoparticles spin state on the MoS$_2$ band structure, additional to the thermal one.[66] On the other hand, the strain generated for the 40 nm nanoparticles in the SCO/MoS$_2$-2a heterostructure exhibits an analogous plot than that of SCO/MoS$_2$-1, showing a lower redshift (~10 meV), Extended Data Fig. 2 and 3. This confirms the reduced strain generated by these smaller nanoparticles.

To further prove that the SCO-NPs induce this effect, we have performed a blank experiment on CE-MoS$_2$ transformed into the semiconducting 2H-phase by thermal treatment, CE-MoS$_2$ (2H).[19] As can be observed in Extended Data Fig. 5, the hysteretic behaviour is absent in this case, being the A peak at each temperature completely independent of the heating or cooling path. These measurements furtherly support the mechanical origin of the electrical and optical SCO/MoS$_2$ properties modulation. In fact, the electronic effect can be considered as negligible since the optical band gap dependence of MoS$_2$ is mostly insensitive to the change in the dielectric environment caused by the spin transition. Thus, theory predicts that a change of few units in the dielectric constant, expected for this SCO material,[67] leads to a shift of ~5 meV, at best, which could not be responsible for the large PL peak redshift observed (~40 meV).[68] Based on previous works,[64] the redshift observed in the SCO/MoS$_2$-1 hybrid inside the temperature interval where the hysteresis loop is observed (i.e. ~40 meV at 355 K) corresponds to a ~0.6% of tensile strain, and for SCO/MoS$_2$-2a (i.e. ~10 meV at 370 K) to a ~0.1%, whereas the observed decrease of the PL intensity in both cases can be attributed to the increase in indirect band gap behaviour of the MoS$_2$ as a consequence of the strain.

Moreover, since the spin transition of the nanoparticles can be triggered by tuning the intensity of an irradiating light, the possibility of using an optical source to drive the PL of the

SCO/MoS$_2$-1 hybrid was evaluated.[65] As shown in Fig. 5c, we measured the A peak of the hybrid at two green laser excitation intensities, 0.08 mW (purple curve), and 0.8 mW (green curve). For the lower intensity, the SCO-NPs in the heterostructure are in the LS state while for the higher one they are expected to undergo a spin transition to the HS state (Extended Data Fig. 6). Under these conditions, SCO/MoS$_2$-1 spectra show that the A peak redshifts of about 60 meV. Besides, once the intensity is normalized respect the counts per second and mW, a clear intensity decrease upon the spin transition is recorded (Supplementary Information Fig. 15 before normalization, Fig. 5c after). Hence, these measurements prove that we can also optically induce a spin transition at room temperature by increasing the power of the excitation laser.

Comparing these results with the PL modulation thermally achieved, the shift of the A peak is clearly higher when a light source is used. This is indicative of a cooperative effect between the heating of the nanoparticles, due to laser irradiation, and the strain induced by the spin transition. Interestingly, when using CE-MoS$_2$ (2H) samples for blank measurements, we observe that under these laser intensities (0.8 and 0.08 mW), the PL remains unaffected (Fig. 5d), suggesting that MoS$_2$ is not directly heated by the laser in these experimental conditions, despite the fact that a thermal heating of the SCO-NPs is expected.[65] These studies thus demonstrate the possibility of inducing strain in the MoS$_2$ by light irradiation, opening the door to the fast optical modulation of 2D material properties. Moreover, as far as the spin state is concerned, it is possible to sense the spin in these SCO-NPs by following the change in the MoS$_2$ luminescence. This result represents on the one hand, an optical detection that cannot be achieved in SCO/graphene heterostructures,[42] and, on the other, a tool for optical identification of spin states which is much more sensitive, simple and local than that obtained from transport measurements.

Discussion

We have reported here a two-step protocol in solution to chemically design smart molecular /2D heterostructures, formed by stimuli-responsive SCO-NPs covalently linked to semiconducting MoS$_2$ flakes. In a first step, chemically exfoliated MoS$_2$ flakes (metallic 1T-phase) have been covalently functionalized with an organic molecule (IPTS). This dramatically alters their electrical and optical properties and restores the semiconducting 2H-MoS$_2$ phase. Then, by means of the use of the attached molecules as grafting points, the SCO-NPs have been homogeneously anchored on these semiconducting MoS$_2$ layers, without further modification of the electronic structure of the 2D system. The robust synthetic methodology developed has

permitted to obtain a family of SCO/MoS$_2$ covalently-linked heterostructures in which a control over the size of the nanoparticles and the degree of surface coverage has been achieved. This has led to a tunability in the resulting properties of the hybrids, which show a strong interplay between the spin transition and MoS$_2$ layers properties, leading to smart heterostructures that respond to external stimuli.

Regarding the 2D component, the change in volume of the SCO-NPs induced by the spin transition upon varying the temperature or by light irradiation, has generated a tensile strain on the MoS$_2$ layers, which has been reflected by sharp changes in their electrical and optical properties. Notice that the present approach is radically different from those previously reported in this area,[26] in which the strain has been generated on pure MoS$_2$ layers by different strategies like the direct application of pressure on a suspended layer, with an AFM tip;[25] by using substrates that can transfer strain to the MoS$_2$ layer by a mechanical bending (in a flexible substrate)[24] or stretching (in an elastomeric substrate);[28] or by applying voltage (in a piezoelectric substrate),[69] or temperature (in a thermo-responsive substrate).[70] In contrast to all these cases, here the strain is self-generated inside a single material, based on a chemically-designed hybrid heterostructure, either by a temperature modulation or by light irradiation. Hence, the intrinsic properties of the SCO component have permitted the use of light as an external and contactless stimulus to induce strain in TMDCs layers and to detect the spin switching.

Additionally, it is important to notice that in contrast to previous methods, the reported approach uses chemically exfoliated MoS$_2$, which permits to have inks of the target SCO/MoS$_2$ system, enabling simpler processability (e.g. by spin coating) than using mechanically exfoliated or CVD grown MoS$_2$ layers. Moreover, the regular dispersion of strain sources all over the 2D material will facilitate a homogeneous strain distribution. These features could simplify the integration of the SCO/MoS$_2$ material in large scale multilayer optoelectronic devices. Additionally, the reported SCO/MoS$_2$ synthesis could also be extended to mechanical/CVD grown layers because it is based on a general procedure i.e.: the nucleophilic attach from the MoS$_2$ to a halide substituted molecule, that can be applied on 2D layers obtained by wet or dry methods without distinction.[53] This will open the possibility of deeper understanding of underlying physical phenomena in further works.

From the point of view of the SCO nanoparticles, the results reported herein open the path for an optical sensing of the spin-state switching in these materials, expanding their use as active components of non-volatile memory devices able to store information near room temperature. In the last decade, the performance and stability of these SCO devices have been investigated.

Thus, in a first step, single-nanoparticle SCO devices were developed,[71] and a few years later, their electronic performance was significantly improved by using 2D assemblies of SCO nanoparticles (ON/OFF values of ca. 300)[57] and very recently with nanoparticles formed by a gold core and an ultra-thin SCO shell (ON/OFF values of ca. 5000).[72] Still, these devices were quickly degraded upon thermal cycling due to the chemical instability of the nanoparticles under working conditions. To overcome this instability problem, they were protected with a silica shell, or deposited on graphene for indirect electrically sensing.[42,73] In the present work, both solutions are combined, giving rise to a robust heterostructure showing large switching effects (ON/OFF values of ca. 900), without any apparent fatigue upon cycling. Therefore, the reported results should be seen as the proof of concept of an innovative approach for the modulation of MoS_2 electrical and optical properties through strain. Further optimization to reach room temperature stimuli-response strainable 2D hybrid materials, with different broadness of the hysteretic behaviour, could be achieved in the next future, by playing with the design of the SCO component. Finally, the fact that the material is prepared in solution may facilitate a future scale-up.

In conclusion, these results demonstrate the fabrication of a multifunctional material where properties of the two components have been reciprocally boosted. Compared to pure SCO-NPs, MoS_2 confers to this hybrid luminescence and higher resilience and conductance. Concurrently, MoS_2 gains new degrees of freedom thanks to SCO-NPs spin, which can be addressed by temperature or light and read-out electrically or optically. Interestingly, our approach could be easily expanded to other 2D materials offering a yet unexplored modulation of their properties and opening new frontiers for strain engineering, towards their application in multifunctional devices beyond conventional electronics.[74]

Methods

Materials. All chemical reagents were purchased and used without further purification: (3-Iodopropyl)trimethoxysilane, 1-Iodooctadecane (Sigma-Aldrich), Tetraethyl orthosilicate 98% (Sigma-Aldrich), Triton X-100 (Sigma-Aldrich), ascorbic acid (Sigma-Aldrich), 1,2,4-triazole (Sigma-Aldrich), iron tetrafluoroborate hexahydrate (Sigma-Aldrich), n-hexanol (Sigma-Aldrich), cyclohexane (Sigma-Aldrich, ethanol absolute (Sigma-Aldrich) ultra-pure water (18.2 MΩ). Molybdenum(IV) sulfide (Alfa Aesar), n-butyllithium solution 1.6 M in hexane (Sigma-

Aldrich), anhydrous hexane (Sigma-Aldrich). SiO_2 (285 nm)/Si substrates were bought from NOVA Electronic Materials LLC, Flower Mound, TX.

Chemical exfoliation MoS₂ (CE-MoS₂). The chemical exfoliation of MoS_2 was carried out according to the experimental protocol reported by M. Morant-Giner et al.[52] A 23-mL Teflon autoclave reactor containing 320.0 mg (2.0 mmol) of commercial $2H$-MoS_2 powder and 5 mL of 1.6 M (8 mmol, 4 eq) *n*-BuLi solution in hexane, previously charged inside a nitrogen-filled glovebox with low water vapour and oxygen levels (< 0.1 ppm), is heated at 100 ºC for 2 h in an oven. After the intercalation reaction, the resulting mixture is filtered and repeatedly washed with hexane inside the glovebox. Once exposed to air, the material collected in the filter is dispersed in 10 mL of degassed Milli-Q water for 1 h in a sonication bath. The dark suspension is purified via dialysis for 16 h to obtain a dispersion with a pH slightly lower than 7. Subsequently, the content of the dialysis is transferred into a centrifuge tube and subjected to a 30-min bath sonication followed by a 30-min centrifugation cycle (750 rpm, 10 ºC). Finally, once separated from the sediment, the supernatant is used without further purification.

Chemical exfoliated MoS₂ in 2H-phase.

CE-MoS_2 flakes retrieved by centrifugation is spin coated on SiO_2 (285 nm)/Si substrates and heated up at 200ºC for 2 h under an inert atmosphere (O_2 < 0.1 ppm, H_2O < 0.1 ppm), to induce the 1T-to-2H-phase transition

70 x 40 nm [Fe(Htrz)(trz)(BF₄)]@SiO₂ Nanoparticles (SCO-NPs, 1). The nanoparticles were synthetized following a strategy very close to that previously reported by R. Torres-Cavanillas et al.[48] but with slight modifications. An aqueous solution of $Fe(BF_4)_2 \cdot 6H_2O$ (0.5 mL, 1.25 M) and tetraethyl orthosilicate (TEOS) (0.1 mL) is added to a freshly prepared mixture containing Triton X-100 (1.8 mL, ω = 9), n-hexanol (1.8 mL), cyclohexane (7.5 mL). A microemulsion of this mixture is obtained by stirring at room temperature for 15 minutes. Then, an aqueous solution of 1,2,4-1H-triazole (0.5 mL, 4.5 M) ligand containing the TEOS (0.1 mL) is added to a similarly prepared organic solution and stirred at room temperature for 15 min. In order to

permit a micellar exchange, both microemulsions are combined and stirred for 2 h. The formed nanoparticles are isolated by precipitation upon addition of acetone and collected by centrifugation (12000 rpm, 10 min), followed by washing with ethanol (x4 times), to remove the excess of surfactant, and acetone (x1 time). Finally, the powdered samples are dried at 70°C for 2 h.

40 x 40 nm [Fe(Htrz)(trz)(BF$_4$)]@SiO$_2$ Nanoparticles (SCO-NPs, 2). The synthesis of the smallest NPs follows the same procedure as for the 70 nm but using 2 mL of Triton X.100.

MoS$_2$ IPTS functionalization (PTS-MoS$_2$). Firstly, a 5 mM aqueous suspension of CE-MoS$_2$ flakes is prepared from the mother one. Independently, a solution of 3-iodopropyl(trimethoxysilane) (IPTS), 0.1 M in ethanol is prepared. Later the IPTS solution is slowly added over the aqueous suspension in water:ethanol ratio, 2:1, under strong stirring, and let it react for 12h. Finally, the functionalized nanosheets are washed by several cycles of centrifugation (at 7000 rpm, 15 min) and dispersed in water:ethanol, 2:1 (x3 times), and in ethanol (x3 times).

SCO/MoS$_2$. The functionalized PTS-MoS$_2$ is suspended in ethanol under vigorous stirring in a concentration of 5 mM. Later, a colloidal suspension of 70 nm SCO-NPs, 10 mg·ml^{-1}, is added and leave it to react for 48 h. Finally, several cycles of centrifugation and dispersion at different rates are carried out until the supernatant has no residues of SCO-NPs. Induced coupled plasma optical emission spectrometry (ICP-OES) of acid-digested samples, indicated a Fe:Mo ratio of 2:1. (SCO/MoS$_2$-**1**). The calculated coverage from TEM images was ~80 %, Supplementary Information **Table 1**.

For the synthesis of the analogue hybrid with smaller size nanoparticles, at different Fe:Mo ratios, an equivalent procedure was followed but adding 40 nm SCO-NPs suspension in 10, 1, or 20 mg·ml^{-1} for: SCO/MoS$_2$-**2a**, SCO/MoS$_2$-**2b** and SCO/MoS$_2$-**2c**, respectively. ICP-OES Fe:Mo ratios of 2:1 for SCO/MoS$_2$-**2a**, 0.4:1 for SCO/MoS$_2$-**2b** and 5:1 for SCO/MoS$_2$-**2c** were measured. The degrees of coverage in the different samples were estimated from TEM images

as ~80 %, ~55 %, and ~100 % for SCO/MoS$_2$-**2a**, **2b**, and **2c**, respectively (Supplementary Information **Table 1**).

Author Contributions

R.T-C. and M.M-G. contributed equally to this work. R. T.-C. was responsible of the design, synthesis and characterization of the new heterostructure and was involved in all the experimental measurements, discussion and preparation of the manuscript. M. M-G was in charge of the preparation of the exfoliated material and help with all characterization steps of the new system. M. G. was in charge of all transport characterization, where G. E-A, J. D. and S. T. were involved. S. C.-S. helped with discussion and theoretical interpretation of the observed properties. M. G.-M. contributed to the SCO-NPs preparation and the discussion and interpretation of results. J. C.-F. was involved in photoluminescence experiments and their interpretation. A. F.-A. designed the work and was involved in the development and coordination of all experimental parts, discussion of results and preparation of the manuscript. E. C. supervised all the work and the preparation of the manuscript. All authors revised and contributed to the presented manuscript.

Competing Interests
The authors declare no competing interests

Supplementary Information
Supplementary Information is available.

Data Availability
The data that support the findings of this study are available within the paper and its supplementary information files and from the corresponding authors upon request.
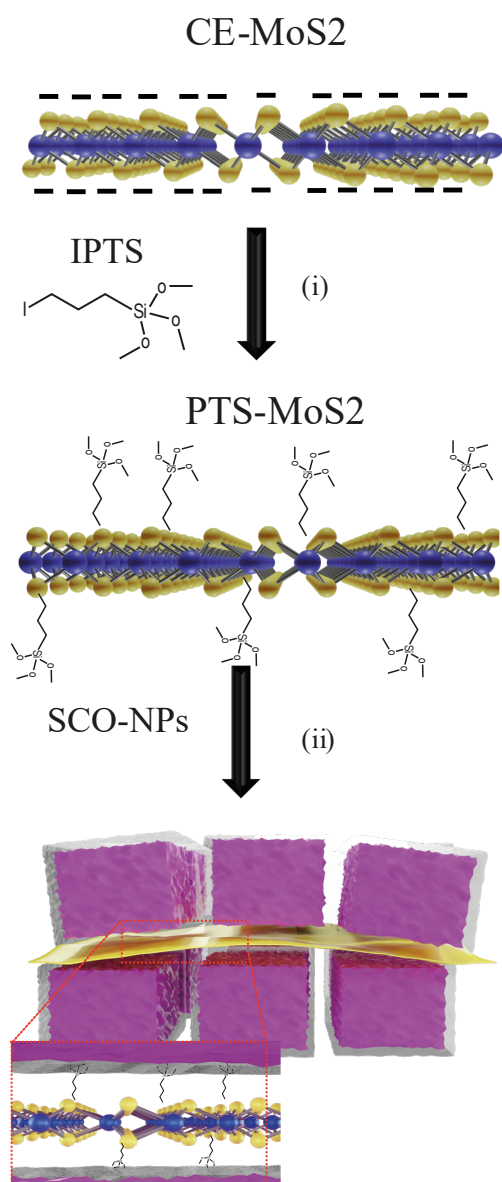
Figure and extended data figure captions

Fig. 1. Schematic representation of the synthetic approach to prepare SCO/MoS$_2$ hybrid heterostructures. (i) CE-MoS$_2$ layer which presents an excess of negative charge on its surface, is covalently functionalized with propyl(trimethoxysilane) (PTS) groups by reaction with 3-iodopropyl(trimethoxysilane) (IPTS). Approximately a 30% of functionalization is reached. Mo atoms are represented in blue and S atoms in yellow; (ii) SCO-NPs which are formed by a [Fe(Htrz)$_2$(trz)](BF$_4$) coordination polymer core represented in pink (Htrz = 1,2,4-triazole and trz = triazolate) and are covered by a thin SiO$_2$ shell represented in grey. SCO-NPs are attached to the functionalized MoS$_2$ layers through covalent bonding between the trimethoxysilane group and the SiO$_2$ shell. Final SCO-NPs coverage depends on the initial SCO-NPs:MoS$_2$ ratios.
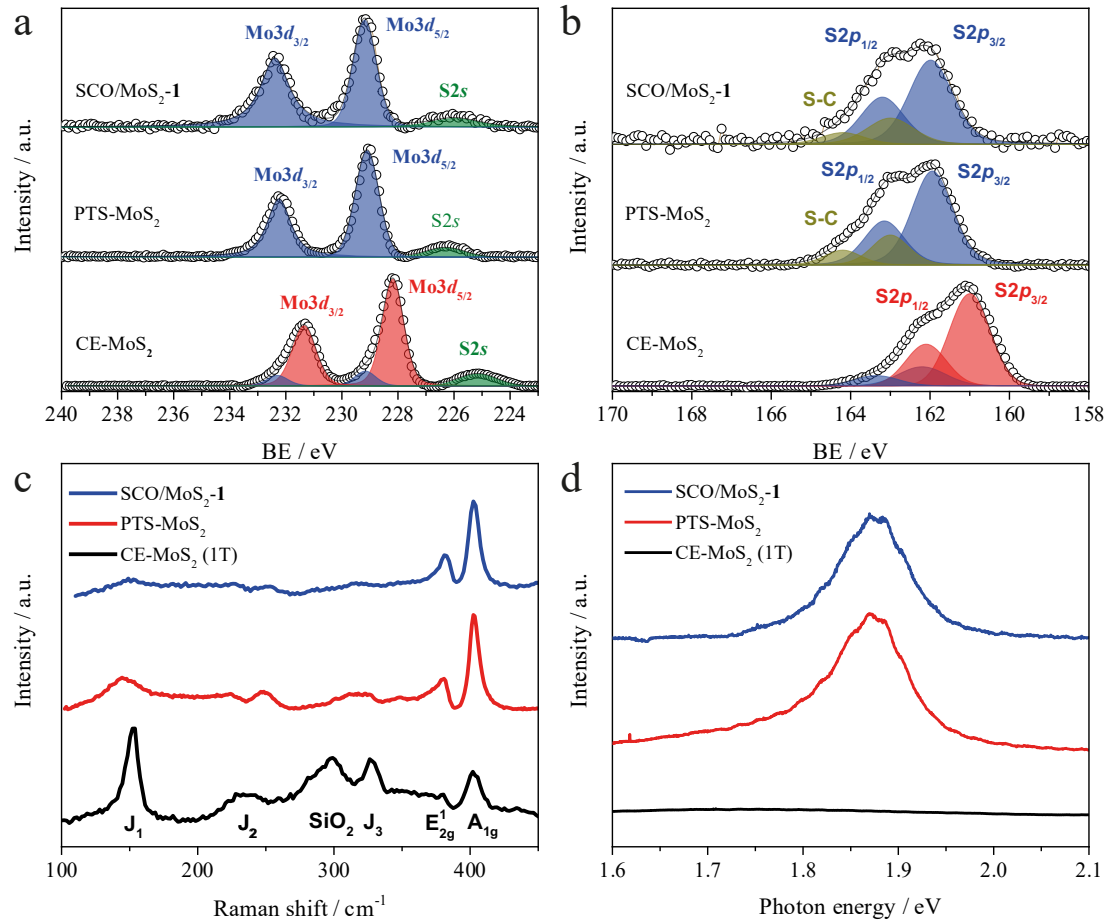
Fig. 2. Spectroscopic characterization of CE-MoS₂, PTS-MoS₂, and SCO/MoS₂-1. a) Mo*3d* and b) S*2p*, deconvoluted high-resolution XPS spectra (blue, 2H-phase and red, 1T-phase contributions). CE-MoS₂ spectra show a main contribution of 1T-MoS₂ phase while after functionalization, PTS-MoS₂ spectra present a clear increase of 2H-phase, which is retained after the attachment of the SCO-NPs (SCO/MoS₂-1). c and d) Raman and PL spectra, respectively, measured with 532 nm excitation wavelength. After MoS₂ functionalization, J peaks in the Raman spectra are not visible, and clear PL appears, supporting XPS conclusions about the conversion from 1T-phase in CE-MoS₂ to 2H-phase in PTS-MoS₂, and SCO/MoS₂-1.
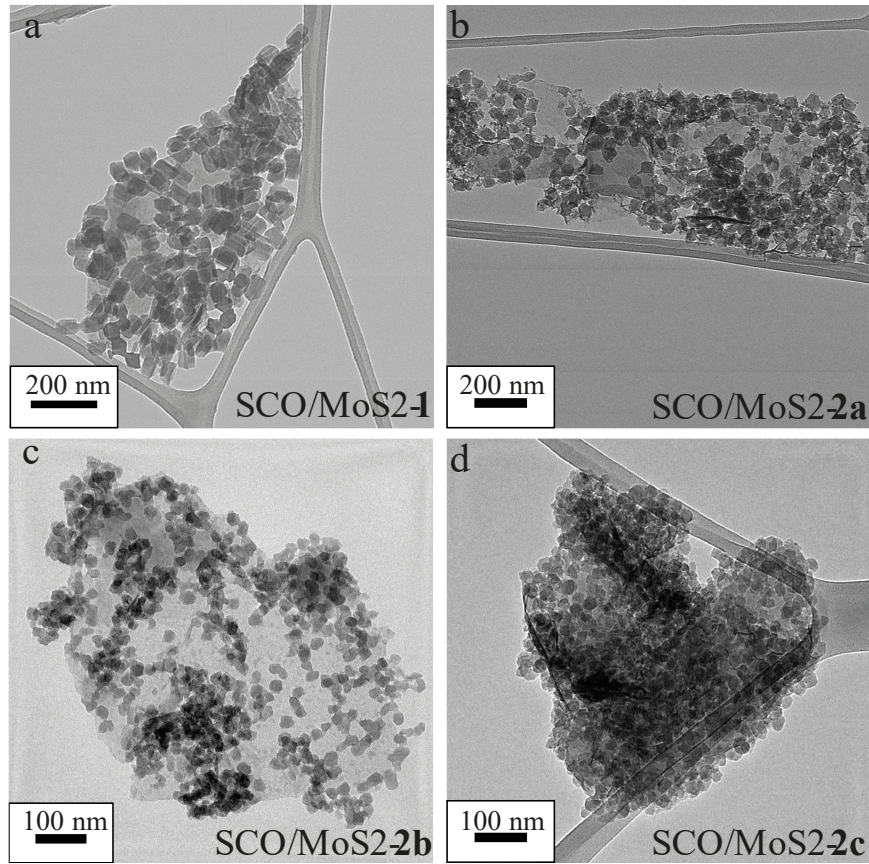
Fig. 3. TEM morphological characterization of SCO/MoS$_2$-1, -2a, -2b and -2c. (a) TEM image of SCO/MoS$_2$-1 showing SCO-NPs of 70 nm on the MoS$_2$ layer with a 78 ± 2% surface coverage. (b), (c) and (d), TEM images of SCO/MoS$_2$-2a, -2b and -2c respectively, showing SCO-NPs of 40 nm on the MoS$_2$ layers with different surface coverages, i.e.: 82 ± 3 % (SCO/MoS$_2$-2a), 50 ± 2 (SCO/MoS$_2$-2b), 100% (SCO/MoS$_2$-2c). Final surface coverages are directly related to the initial SCO-NPs:MoS$_2$ ratios in the synthetic protocol.
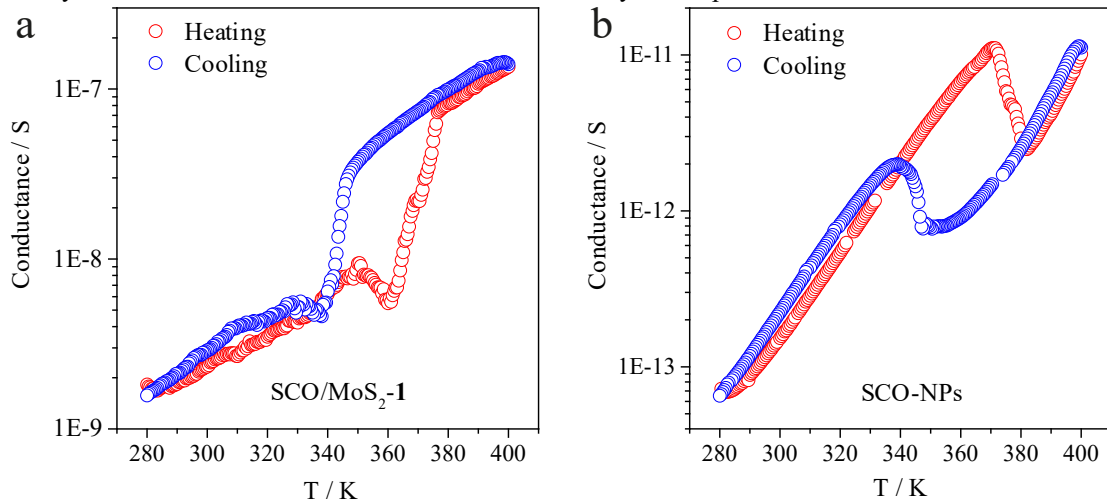
Fig. 4. Transport measurements. Thermal variation of the conductance in the heating and cooling modes for SCO/MoS$_2$-1, (a) and bare SCO-NPs, (b). The applied voltages were 2 V and 100 V, respectively. Thermal ramp was performed at 1 K·min^{-1}. The hybrid material presents a much higher conductivity than the pure SCO-NPs, indicating that in this case, the conductivity occurs through the MoS$_2$ layers. Both materials present sharp drops and increases in conductance at the spin transition temperatures, which points out to the direct relation between the conductivity changes and the spin-transition of the SCO-NPs. The hybrid material (a) is more conductive when the SCO-NPs attached on the MoS$_2$ layers are in HS than when they are in LS, while for pure SCO-NPs (b) the opposite behaviour is observed, and pure SCO-NPs are less conductive in the HS than in the LS. Thus, this supports the idea that in the composite, transport goes through the MoS$_2$ layers and the changes observed in the electronic properties of the MoS$_2$ flakes are driven by the spin state of the attached SCO-NPs. It is known that the change in spin state of the nanoparticles involves a volume change that is expected to strain the underlaying MoS$_2$ layers modulating their electronic structure.
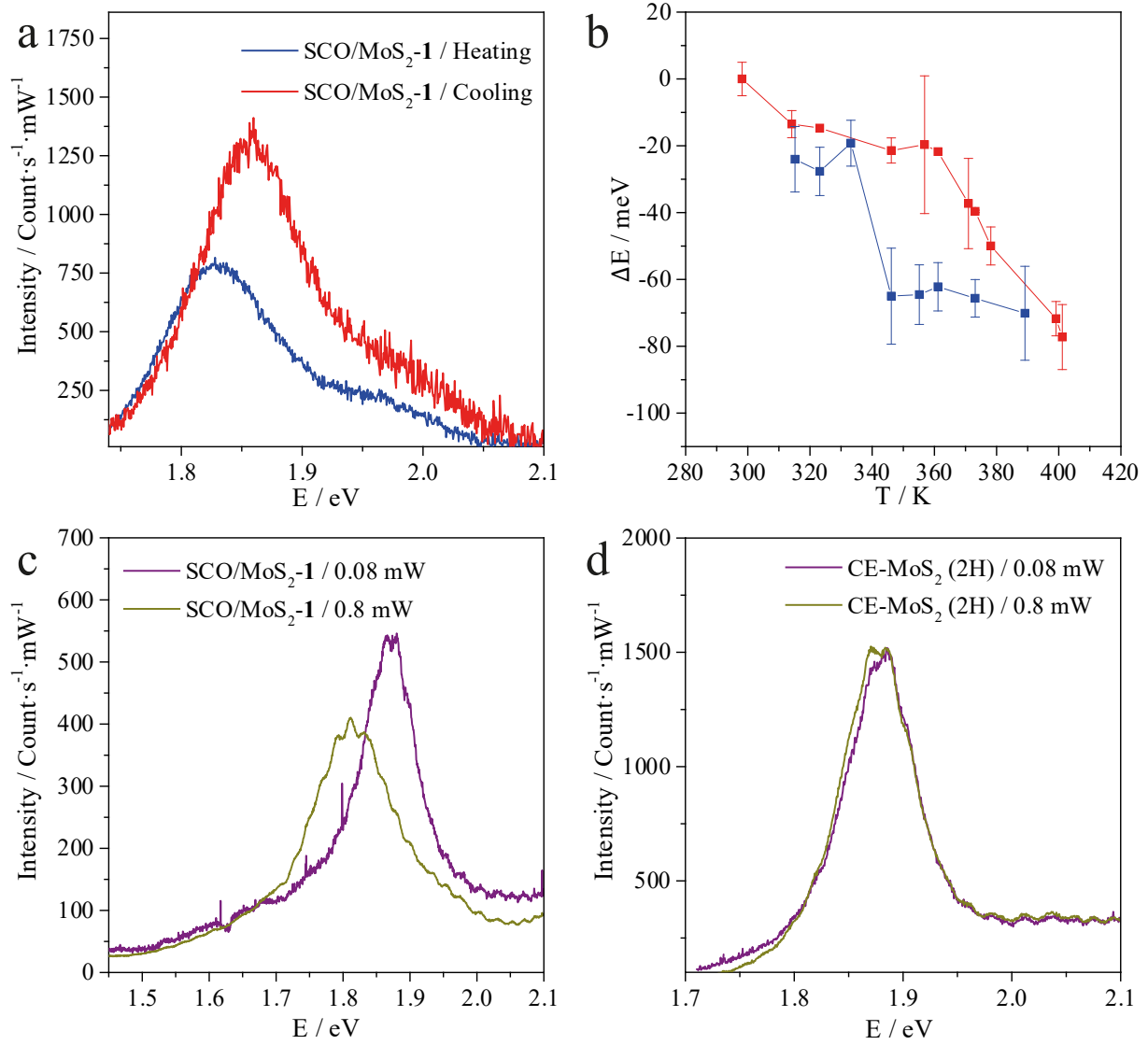
Fig. 5. Photoluminescence measurements. (a) PL spectra of SCO/MoS$_2$-1 at LS, red line (heating), and HS states, blue line (cooling), taken at 355 K and 0.08 mW. (b) PL shift as a function of temperature, measured at 0.08 mW (red dots, heating and blue dots, cooling); error bars represent standard deviation of the average PL shifts measured for 9 flakes at each temperature. Both panels highlight the hysteretic behaviour presented by the position of SCO/MoS$_2$-1 PL maxima under subsequent heating and cooling processes, resembling that showed by SCO-NPs spin transition with temperature. (c) and (d) PL spectra at two different laser intensities (0.8 mW, green and 0.08 mW, purple) of SCO/MoS$_2$-1 and reference sample CE-MoS$_2$ (2H), respectively (all the intensities have been normalized to the acquisition time and the power of the excitation laser). These measurements prove that optical induced spin transition can modulate MoS$_2$ PL spectrum. All spectra were measured with 532 nm excitation wavelength. Different PL features displayed by Fig. 5a and c are related to the quality of the flakes. More defective flakes exhibit a lower A peak, allowing the visualization of the B peak. [63]
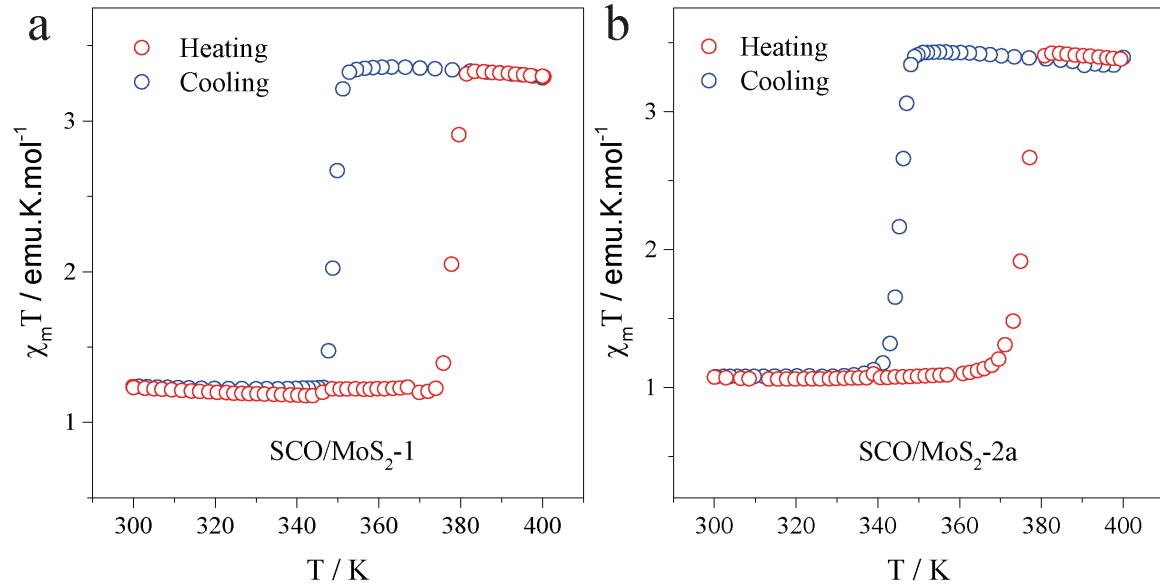
Extended Data Fig. 1 | Magnetic characterization of the composites. a,b, Thermal variation of the $\chi_M T$ product for the SCO/MoS$_2$-**1** (a) and SCO/MoS$_2$-**2a** (b). In both cases, the $\chi_M T$ value increases at the transition temperature from LS to HS, ulteriorly recovering its initial value with the reverse transition supporting the integrity of the SCO-NPs in the composites. χ_M, molar magnetic susceptibility.
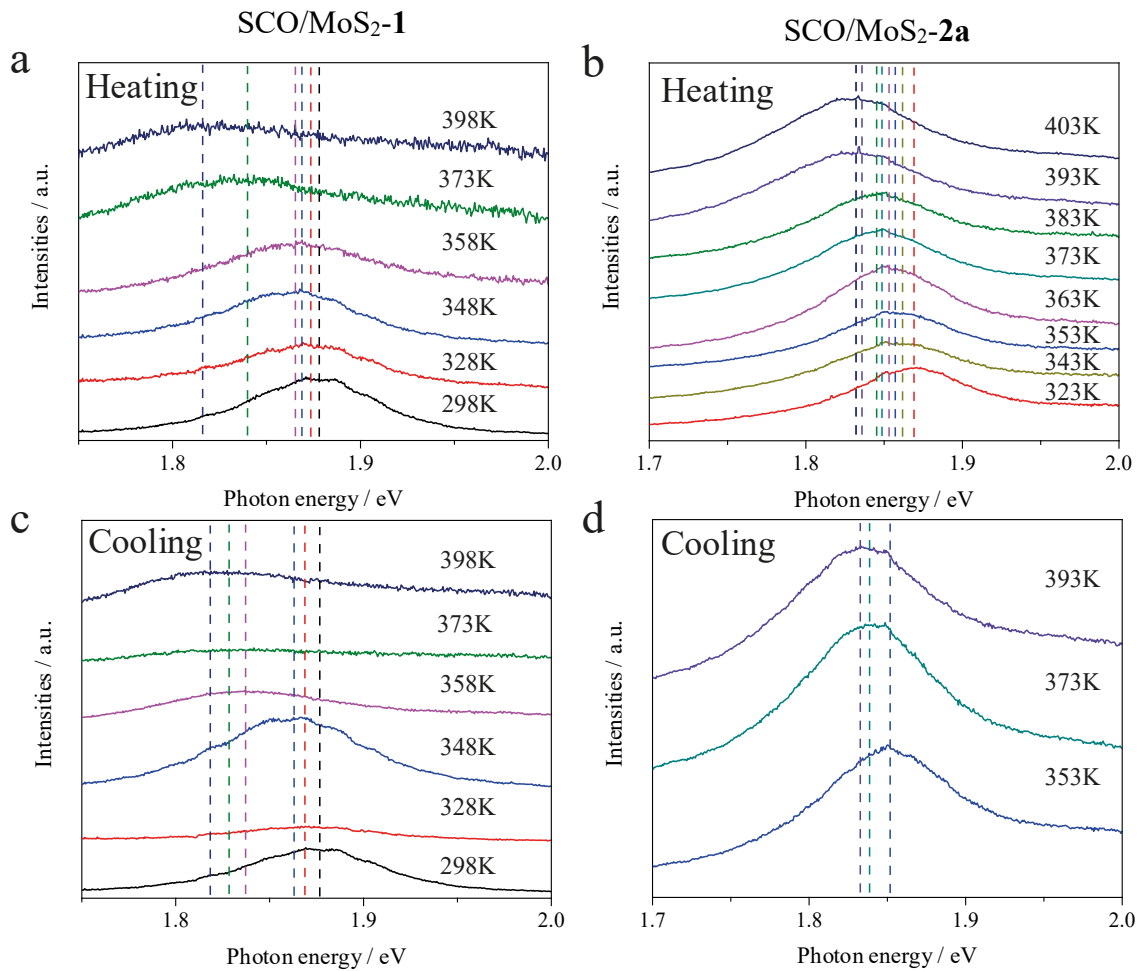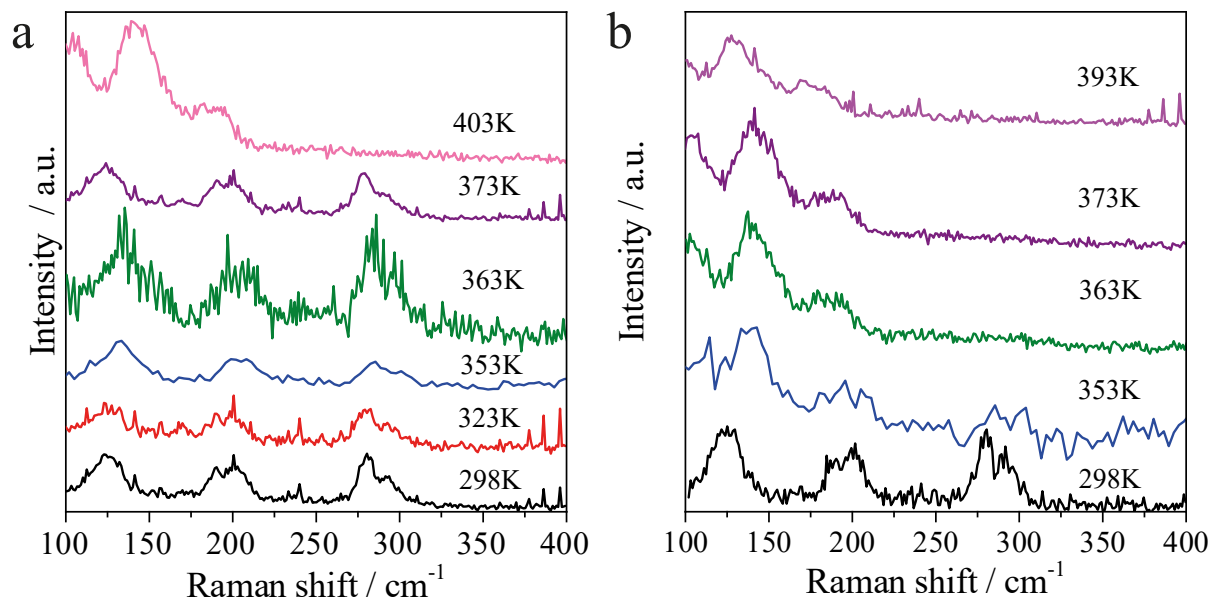

Extended Data Fig. 2 | Temperature-dependent photoluminescence of the composites. a-d, Evolution of the PL emission maximum with the temperature of SCO/MoS$_2$-1 (left panels) and SCO/MoS$_2$-2a (right panels) during the heating (a,b) and the cooling (c,d) processes. The excitation power was fixed at 0.08 mW/μm$_2$ to avoid thermal interferences. At any temperature between spin transition temperatures (380-340 K), the A peak position depends

on the SCO-NPs spin state for both samples (that is, on the heating or cooling process), shifting to lower values in the HS (cooling process). This effect is observed to be more substantial for SCO/MoS$_2$-**1**.
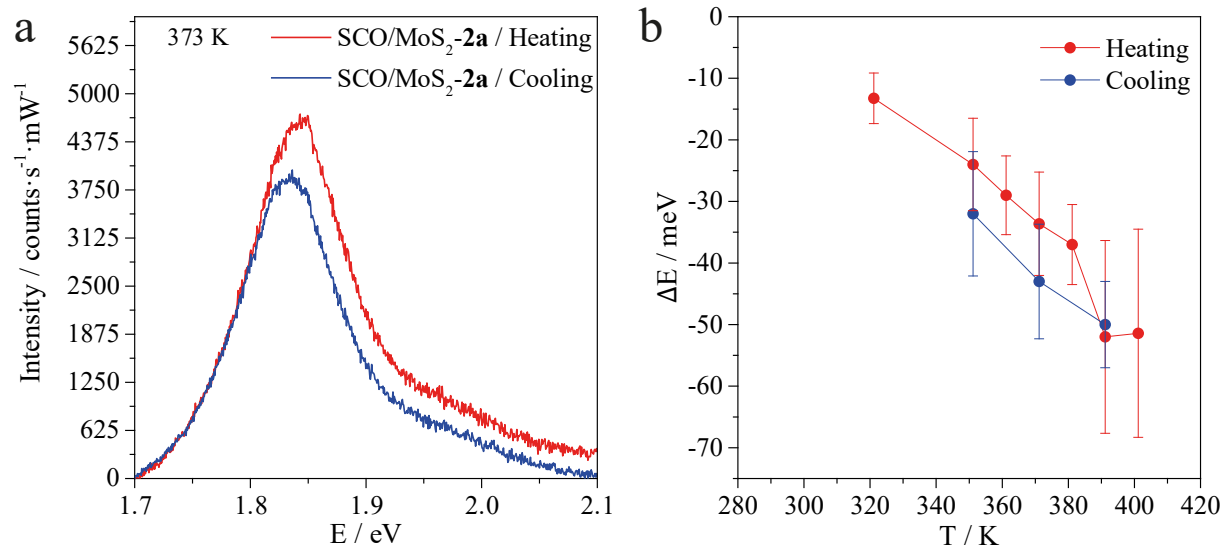

Extended Data Fig. 3 | SCO/MoS$_2$-2 optical response. a, PL spectra of SCO/MoS$_2$-2a at LS (red line, heating), and HS states (blue line, cooling), taken at 373 K and 0.08 mW. Clearly the HS state displays an A peak located at lower energy due to the strain applied by the SCO-NPs with increased volume after spin transition. b, PL shift as a function of the temperature (red dots, heating and blue dots, cooling). The position of the A peak of the MoS$_2$ reflects the hysteretical behaviour of the SCO-NPs spin transition. Error bars represent the standard deviation calculated from at least three different areas measured at each temperature.

Extended Data Fig. 4 | Temperature-dependent Raman spectra of the SCO-NPs. a,b, Raman spectra of the SCO-NPs at different temperatures during the heating (a) and cooling (b) processes. The Raman spectra change depending on the SCO-NPs spin state.
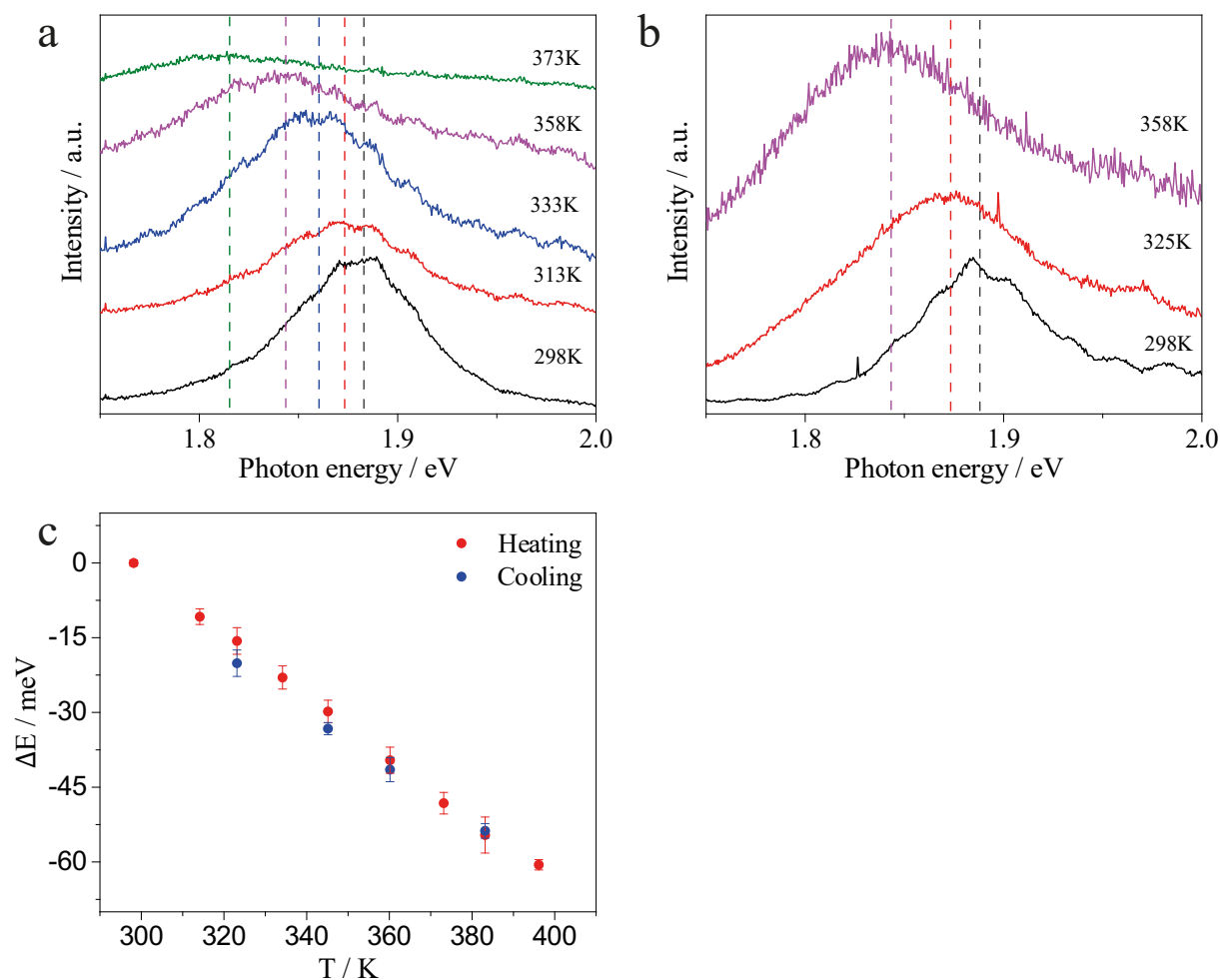
Extended Data Fig. 5 | Temperature-dependent photoluminescence of the CE-MoS$_2$(2H). a,b, Evolution of the PL emission maximum with the temperature of phase converted CE-MoS$_2$(2H) during the heating (a) and the cooling (b) processes. **c,** PL maximum shifts as a function of temperature (red dots, heating and blue dots, cooling). The position of the PL maximum exhibits a linear displacement with the temperature. Processed error bars represent standard deviation calculated from at least three different areas measured at each temperature. Excitation power at 0.08 mW/µm^2.
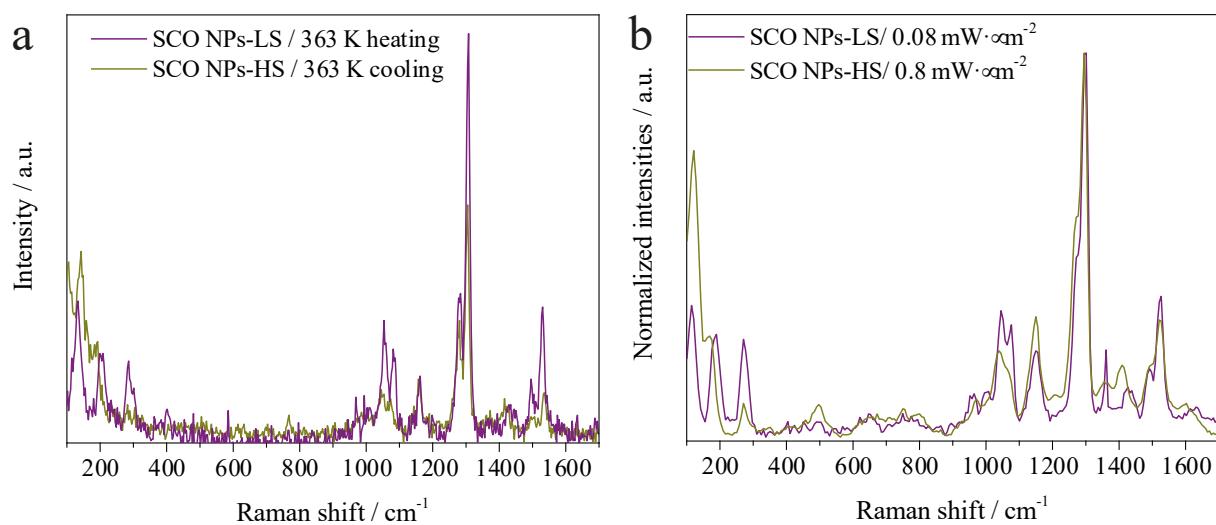
Extended Data Fig. 6 | Raman spectra of the SCO-NPs upon light irradiation. SCO-NPs Raman spectra at different conditions. **a,** Temperature: 363 K and laser intensity 0.08 mW (inside SCO-NPs hysteresis between spin transition temperatures), during the heating (LS, purple) and the cooling (HS, yellow) processes. **b,** At room temperature with two different laser intensities: 0.08 mW (purple) and 0.8 mW (yellow), exhibiting the typical spectrum of the LS and HS states, respectively.

1. Stanford, M. G., Rack, P. D. & Jariwala, D. Emerging nanofabrication and quantum confinement techniques for 2D materials beyond graphene. *npj 2D Materials and Applications* **2,** 768–15 (2018).

2. Wang, L. *et al.* One-Dimensional Electrical Contact to a Two-Dimensional Material. *Science* **342,** 614–617 (2013).

3. Xia, W. *et al.* Recent progress in van der Waals heterojunctions. *Nanoscale* **9,** 4324–4365 (2017).

4. Onga, M. *et al.* Antiferromagnet-Semiconductor Van Der Waals Heterostructures: Interlayer Interplay of Exciton with Magnetic Ordering. *Nano Lett.* **20,** 4625–4630 (2020).

5. Hirsch, A. & Hauke, F. Post-Graphene 2D Chemistry: The Emerging Field of Molybdenum Disulfide and Black Phosphorus Functionalization. *Angew. Chem. Int. Ed.* **57,** 4338–4354 (2018).

6. López-Cabrelles, J. *et al.* Isoreticular two-dimensional magnetic coordination polymers prepared through pre-synthetic ligand functionalization. *Nature Chemistry* **10,** 1001–1007 (2018).

7. Rodríguez-San-Miguel, D., Montoro, C. & Zamora, F. Covalent organic framework nanosheets: Preparation, properties and applications. *Chem. Soc. Rev.* **49,** 2291–2302 (2020).

8. Zhao, Y., Bertolazzi, S. & Samorì, P. A Universal Approach toward Light-Responsive Two-Dimensional Electronics: Chemically Tailored Hybrid van der Waals Heterostructures. *ACS Nano* **13,** 4814–4825 (2019).

9. Jariwala, D., Marks, T. J. & Hersam, M. C. Mixed-dimensional van der Waals heterostructures. *Nat Mater* **16,** 170–181 (2017).

10. Choi, J., Zhang, H. & Choi, J. H. Modulating Optoelectronic Properties of Two-Dimensional Transition Metal Dichalcogenide Semiconductors by Photoinduced Charge Transfer. *ACS Nano* **10,** 1671–1680 (2016).

11. Das, S., Robinson, J. A., Dubey, M., Terrones, H. & Terrones, M. in *Annual Review of Materials Research* **45,** 1–27 (2015).

12. Manzeli, S., Ovchinnikov, D., Pasquier, D., Yazyev, O. V. & Kis, A. 2D transition metal dichalcogenides. *Nat. Rev. Mater.* **2,** (2017).

13. Two-dimensional transition metal dichalcogenides: interface and defect engineering. *Chem. Soc. Rev.* **47,** 1–29 (2018).

14. Ganatra, R. & Zhang, Q. Few-layer MoS_2: A promising layered semiconductor. *ACS Nano* **8,** 4074–4099 (2014).

15. Kan, M. *et al.* Structures and phase transition of a MoS_2 monolayer. *J. Phys. Chem. C* **118,** 1515–1522 (2014).

16. Wang, L., Xu, Z., Wang, W. & Bai, X. Atomic mechanism of dynamic electrochemical lithiation processes of MoS_2 nanosheets. *J. Am. Chem. Soc.* **136,** 6693–6697 (2014).

17. Yuwen, L. *et al.* Rapid preparation of single-layer transition metal dichalcogenide nanosheets via ultrasonication enhanced lithium intercalation. *Chem. Commun.* **52,** 529–532 (2015).

18. Lin, Y.-C., Dumcenco, D. O., Huang, Y.-S. & Suenaga, K. Atomic mechanism of the semiconducting-to-metallic phase transition in single-layered MoS_2. *Nature Nanotech* **9,** 391–396 (2014).

19. Eda, G. *et al.* Photoluminescence from chemically exfoliated MoS_2. *Nano Lett.* **11,** 5111–5116 (2011).

20. Fan, X. *et al.* Fast and Efficient Preparation of Exfoliated 2H MoS_2 Nanosheets by Sonication-Assisted Lithium Intercalation and Infrared Laser-Induced 1T to 2H Phase Reversion. *Nano Lett.* **15,** 5956–5960 (2015).

21. Yang, D., Sandoval, S. J., Divigalpitiya, W. M. R., Irwin, J. C. & Frindt, R. F. Structure of single-molecular-layer MoS2. *Phys. Rev. B* **43,** 12053–12056 (1991).

22. Yun, W. S., Han, S. W., Hong, S. C., Kim, I. G. & Lee, J. D. Thickness and strain effects on electronic structures of transition metal dichalcogenides: 2H-MX$_2$ semiconductors (M = Mo, W; X = S, Se, Te). *Phys. Rev. B Condens. Matter Mater. Phys.* **85,** 033305 (2012).

23. Ouyang, B., Xiong, S., Yang, Z., Jing, Y. & Wang, Y. MoS$_2$ heterostructure with tunable phase stability: Strain induced interlayer covalent bond formation. *Nanoscale* **9,** 8126–8132 (2017).

24. Conley, H. J. *et al.* Bandgap Engineering of Strained Monolayer and Bilayer MoS 2. *Nano Lett.* **13,** 3626–3630 (2013).

25. Manzeli, S., Allain, A., Ghadimi, A. & Kis, A. Piezoresistivity and Strain-induced Band Gap Tuning in Atomically Thin MoS<inf>2</inf>. *Nano Lett.* **15,** 5330–5335 (2015).

26. Sun, Y. & Liu, K. Strain engineering in functional 2-dimensional materials. *J Appl Phys* **125,** 082402–12 (2019).

27. Yang, R. *et al.* Tuning Optical Signatures of Single- and Few-Layer MoS 2by Blown-Bubble Bulge Straining up to Fracture. *Nano Lett.* **17,** 4568–4575 (2017).

28. Castellanos-Gomez, A. *et al.* Local strain engineering in atomically thin MoS$_2$. *Nano Lett.* **13,** 5361–5366 (2013).

29. Tsai, M.-Y. *et al.* Flexible MoS<inf>2</inf> Field-Effect Transistors for Gate-Tunable Piezoresistive Strain Sensors. *ACS Appl. Mater. Interfaces* **7,** 12850–12855 (2015).

30. Biccai, S. *et al.* Negative Gauge Factor Piezoresistive Composites Based on Polymers Filled with MoS$_2$ Nanosheets. *ACS Nano* **13,** 6845–6855 (2019).

31. Urakawa, A. *et al.* Combined, modulation enhanced X-ray powder diffraction and raman spectroscopic study of structural transitions in the spin crossover material [Fe(Htrz)$_2$(trz)](BF$_4$). *J. Phys. Chem. C* **115,** 1323–1329 (2011).

32. Gütlich, P. & Goodwin, H. A. *Spin Crossover in Transition Metal Compounds I.* **233,** 1–356 (2009).

33. Grosjean, A. *et al.* Crystal structures and spin crossover in the polymeric material [Fe(Htrz)$_2$(trz)](BF$_4$) including coherent-domain size reduction effects. *Eur. J. Inorg. Chem.* 796–802 (2013). doi:10.1002/ejic.201201121

34. Dugay, J. *et al.* Sensing of the Molecular Spin in Spin-Crossover Nanoparticles with Micromechanical Resonators. *J. Phys. Chem. C* **123,** 6778–6786 (2019).

35. Coronado, E., Galán-Mascarós, J. R., Monrabal-Capilla, M., García-Martínez, J. & Pardo-Ibáñez, P. Bistable Spin-Crossover Nanoparticles Showing Magnetic Thermal Hysteresis near Room Temperature. *Adv Mater* **19,** 1359–1361 (2007).

36. Rotaru, A. *et al.* Spin state dependence of electrical conductivity of spin crossover materials. *Chem. Commun.* **48,** 4163–4165 (2012).

37. Boldog, I. *et al.* Spin-crossover nanocrystals with magnetic, optical, and structural bistability near room temperature. *Angew. Chem. Int. Ed.* **47,** 6433–6437 (2008).

38. Shepherd, H. J. *et al.* Molecular actuators driven by cooperative spin-state switching. *Nat. Commun.* **4,** 8434–9 (2013).

39. Koo, Y.-S. & Galán-Mascarós, J. R. Spin Crossover Probes Confer Multistability to Organic Conducting Polymers. *Adv Mater* **26,** 6785–6789 (2014).

40. Chen, Y.-C., Meng, Y., Ni, Z.-P. & Tong, M.-L. Synergistic electrical bistability in a conductive spin crossover heterostructure. *J. Mater. Chem. C* **3,** 945–949 (2015).

41. Rat, S. *et al.* Coupling Mechanical and Electrical Properties in Spin Crossover Polymer Composites. *Adv Mater* **30,** 1705275–6 (2018).

42. Dugay, J. *et al.* Phase Transitions in Spin-Crossover Thin Films Probed by Graphene Transport Measurements. *Nano Lett.* **17,** 186–193 (2017).

43.   Geest, E. P. *et al.* Contactless Spin Switch Sensing by Chemo-Electric Gating of Graphene. *Adv. Mater. (Weinheim, Ger.)* **32,** 1903575–9 (2020).

44.   Konstantinov, N. *et al.* Electrical read-out of light-induced spin transition in thin film spin crossover/graphene heterostructures. *J. Mater. Chem. C* **9,** 2712–2720 (2021).

45.   Titos-Padilla, S., Herrera, J. M., Chen, X.-W., Delgado, J. J. & Colacio, E. Bifunctional hybrid SiO_2 nanoparticles showing synergy between core spin crossover and shell luminescence properties. *Angew. Chem. Int. Ed.* **50,** 3290–3293 (2011).

46.   Herrera, J. M. *et al.* Studies on bifunctional Fe(II)-triazole spin crossover nanoparticles: Time-dependent luminescence, surface grafting and the effect of a silica shell and hydrostatic pressure on the magnetic properties. *J. Mater. Chem. C* **3,** 7819–7829 (2015).

47.   Giménez-Marqués, M., García-Sanz de Larrea, M. L. & Coronado, E. Unravelling the chemical design of spin-crossover nanoparticles based on iron(II)-triazole coordination polymers: Towards a control of the spin transition. *J. Mater. Chem. C* **3,** 7946–7953 (2015).

48.   Torres-Cavanillas, R. *et al.* Downsizing of robust Fe-triazole@SiO 2spin-crossover nanoparticles with ultrathin shells. *Dalton Trans.* **1,** 1–5 (2019).

49.   Ulman, A. Formation and Structure of Self-Assembled Monolayers. *Chem. Rev.* **96,** 1533–1554 (1996).

50.   Joensen, P., Frindt, R. F. & Morrison, S. R. Single-layer MoS2. *Mat. Res. Bull.* **21,** 457–461 (1986).

51.   Leng, K. *et al.* Phase Restructuring in Transition Metal Dichalcogenides for Highly Stable Energy Storage. *ACS Nano* **10,** 9208–9215 (2016).

52.   Morant-Giner, M. *et al.* Prussian Blue@MoS_2Layer Composites as Highly Efficient Cathodes for Sodium- and Potassium-Ion Batteries. *Adv. Funct. Mater.* **28,** 1706125 (2017).

53.   Voiry, D. *et al.* Covalent functionalization of monolayered transition metal dichalcogenides by phase engineering. *Nature Chemistry* **7,** 45–49 (2015).

54.   Saito, R., Tatsumi, Y., Huang, S., Ling, X. & Dresselhaus, M. S. Raman spectroscopy of transition metal dichalcogenides. *J Phys Condens Matter* **28,** (2016).

55.   Pramoda, K. *et al.* Nanocomposites of C3N4with Layers of MoS 2and Nitrogenated RGO, Obtained by Covalent Cross-Linking: Synthesis, Characterization, and HER Activity. *ACS Appl. Mater. Interfaces* **9,** 10664–10672 (2017).

56.   Pramoda, K., Gupta, U., Ahmad, I., Kumar, R. & Rao, C. N. R. Assemblies of covalently cross-linked nanosheets of MoS_2 and of MoS_2-RGO: Synthesis and novel properties. *J. Mater. Chem. A* **4,** 8989–8994 (2016).

57.   Dugay, J. *et al.* Spin switching in electronic devices based on 2D assemblies of spin-crossover nanoparticles. *Adv Mater* **27,** 1288–1293 (2015).

58.   Dugay, J. *et al.* Charge Mobility and Dynamics in Spin-Crossover Nanoparticles Studied by Time-Resolved Microwave Conductivity. *Journal of Physical Chemistry Letters* **9,** 5672–5678 (2018).

59.   Rotaru, A. *et al.* Nano-electromanipulation of spin crossover nanorods: Towards switchable nanoelectronic devices. *Adv Mater* **25,** 1745–1749 (2013).

60.   Molnár, G., Rat, S., Salmon, L., Nicolazzi, W. & Bousseksou, A. Spin Crossover Nanomaterials: From Fundamental Concepts to Devices. *Adv Mater* **30,** (2018).

61.   Roldán, R., Castellanos-Gomez, A., Cappelluti, E. & Guinea, F. Strain engineering in semiconducting two-dimensional crystals. *J Phys Condens Matter* **27,** (2015).

62.   Splendiani, A. *et al.* Emerging Photoluminescence in Monolayer MoS 2. *Nano Lett.* **10,** 1271–1275 (2010).

63. McCreary, K. M., Hanbicki, A. T., Sivaram, S. V. & Jonker, B. T. A- and B-exciton photoluminescence intensity ratio as a measure of sample quality for transition metal dichalcogenide monolayers. *APL Mater.* **6,** (2018).

64. Pető, J. *et al.* Moderate strain induced indirect bandgap and conduction electrons in MoS_2 single layers. *npj 2D Materials and Applications* **3,** 5836–6 (2019).

65. Guillaume, F. *et al.* Photoswitching of the spin crossover polymeric material [Fe(Htrz)$_2$(trz)](BF$_4$) under continuous laser irradiation in a Raman scattering experiment. *Chemical Physics Letters* **604,** 105–109 (2014).

66. Korn, T., Heydrich, S., Hirmer, M., Schmutzler, J. & Schller, C. Low-temperature photocarrier dynamics in monolayer MoS_2. *Appl Phys Lett* **99,** (2011).

67. Lefter, C. *et al.* Dielectric and charge transport properties of the spin crossover complex [Fe(Htrz) 2(trz)](BF 4). *Phys. Status Solidi RRL* **8,** 191–193 (2013).

68. Chaves, A. *et al.* Bandgap engineering of two-dimensional semiconductor materials. *npj 2D Materials and Applications* **4,** 1–21 (2020).

69. Hui, Y. Y. *et al.* Exceptional tunability of band energy in a compressively strained trilayer MoS_2 sheet. *ACS Nano* **7,** 7126–7131 (2013).

70. Gant, P. *et al.* A strain tunable single-layer MoS_2 photodetector. *Materials Today* **27,** 8–13 (2019).

71. Prins, F., Monrabal-Capilla, M., Osorio, E. A., Coronado, E. & Van Der Zant, H. S. J. Room-temperature electrical addressing of a bistable spin-crossover molecular system. *Adv Mater* **23,** 1545–1549 (2011).

72. Torres-Cavanillas, R. *et al.* Design of Bistable Gold@Spin-Crossover Core–Shell Nanoparticles Showing Large Electrical Responses for the Spin Switching. *Adv Mater* **31,** 1900039 (2019).

73. Holovchenko, A. *et al.* Near Room-Temperature Memory Devices Based on Hybrid Spin-Crossover@SiO_2Nanoparticles Coupled to Single-Layer Graphene Nanoelectrodes. *Adv Mater* **28,** 7228–7233 (2016).

74. Coronado, E. Molecular magnetism: from chemical design to spin control in molecules, materials and devices. *Nat. Rev. Mater.* **5,** 87–104 (2020).

Supplementary Information

Spin-crossover nanoparticles anchored on MoS_2 layers for heterostructures with tunable strain driven by thermal or light-induced spin switching

Ramón Torres-Cavanillas, Marc Morant-Giner, Garin Escorcia-Ariza, Julien Dugay, Josep Canet-Ferrer, Sergio Tatay, Salvador Cardona-Serra, Mónica Giménez-Marqués, Marta Galbiati, Alicia Forment-Aliaga, Eugenio Coronado

Additional Supporting Information Material: Movie 1.

The video shows the volume modulation upon the spin transition of SCO-NPs **1**, deposited on a Si/SiO$_2$ substrate. The temperature was increased or decreased in 25 ºC steps, letting the sample thermalize for 5 min. For clarity, the original movie, has been accelerated 10 times.

Experimental section

Characterization techniques: Equipment and experimental conditions.

Transmission electron microscopy (TEM): TEM studies were carried out on a Technai G2 F20 microscope operating at 200 kV and a JEM-1010 operating at 100 kV at the Central Service for Experimental Research of the University of Valencia. Samples were prepared by dropping suspensions on lacey formvar/carbon copper grids (300 mesh).

Zeta Potential (ξ) measurements: ξ values were measured at room temperature with a Zetasizer Nano ZS instrument (Malvern Instruments Ltd.).

Thermogravimetric analysis (TGA): Samples were measured using a TGA 550 (TA Instruments) at a heating rate of 5 °C/min from 25-700 °C under air.

Attenuated total reflectance Fourier-transform infrared spectra (ATR-FTIR): Samples were measured using an ALPHA II FTIR Spectrometer (Bruker) in the 4000-400 cm^{-1} range with a resolution of 4 cm^{-1}.

X-ray Photoelectron Spectroscopy (XPS): Samples were analyzed *ex-situ* at the X-ray Spectroscopy Service at the University of Alicante and at the ICMol of the University of Valencia using a K-ALPHA Thermo Scientific spectrometer. All spectra were collected using Al Kα radiation (1486.6 eV), monochromatized by a twin crystal monochromator, yielding a focused X-ray spot (elliptical in shape with a major axis length of 400 or 200 μm) at 30 mA and 2 kV. The alpha hemispherical analyzer was operated in the constant energy mode with survey scan pass energies of 200 eV to measure the whole energy band and 50 eV in a narrow scan to selectively measure the particular elements. XPS data were analyzed with Origin and Avantage sofwares. A smart background function was used to approximate experimental backgrounds. Charge compensation was achieved with the system flood gun that provides low energy electrons and low energy argon ions from a single source.

Transport measurements: All transport measurements have been performed in a Physical Properties Measurement System (Quantum Design, PPMS-9) in the temperature range of 280 K to 400 K, under vacuum. Disc-shaped pressed powder pellets of the different samples were

prepared by applying ca. 0.05 MPa and measured in a two probes configuration. The pellets were contacted through silver paste and Pt wires, maintaining a very close geometry in all samples. Electrical measurements were performed using a Keithley 6517B electrometer as voltage source and to measure current. Conductivity values were calculated as $\sigma = (G \cdot l)/(t \cdot w)$, where G is the measured conductance, l is the distance between electrodes, w the electrodes length, and t the thickness of the pellets. Optical microscopy has been used to estimate these values.

Inductively Coupled-Plasma Optical Emission Spectrometry (ICP-OES): ICP-OES analysis was conducted at the Central Service for Experimental Research of the University of Valencia. Samples were digested in nitric acid using a high-pressure microwave oven.

Magnetic susceptibility (SQUID): Magnetic susceptibility measurements were performed on powdered samples with a Quantum Design MPMS-XL-5 SQUID susceptometer. The susceptibility data were corrected from the diamagnetic contributions and deduced by using Pascal's constant tables. The data were collected in the range 300–400 K upon recording several heating-cooling cycles at a constant rate of 1 K·min^{-1} with an applied field of 0.1 T.

Raman measurements: the Raman measurements were carried out with a Horiba-MTB Xplora at the Central Service for Experimental Research of the University of Valencia. All the samples were measured under continuous wave operation (CW), exciting the sample at 532 nm wavelength. The excitation power was 0.8 or 0.08 mW. The light was focused on the sample using a regular microscope objective (100x magnification, Olympus brand, with a working distance of 0.21 mm). The power was measured placing a laser power meter (Maxlab-TOP from Coherent Inc.) below the objective. SCO-NPs spectra were measured on powdered samples, while the MoS_2 and the SCO/MoS_2 hybrid material were spin-coated on silicon substrates and the largest and most isolated flakes were chosen. The temperature dependent Raman characterization has been carried out by adapting the sample holder of our confocal setup for holding a ceramic resistor of 20 W with one inch^2 area. The sample is located at the centre of the resistor and held with a scotch tape. The temperature of the system is monitored with a platinum resistance and controlled with feedback electronics with a nominal precision of 0.1 K. A stabilization time of five minutes is left between consecutive measurements in the temperature sweep followed for a mapping and a Z scan to minimize eventual thermal drifts.

Zeta-potential measurements

The samples were prepared by dispersing CE-MoS$_2$ or PTS-MoS$_2$ in a mixture 2:1, H$_2$O:EtOH, in a concentration 3 mM of MoS$_2$. The values are shown in Figure 1, and the weighted arithmetic mean provided.
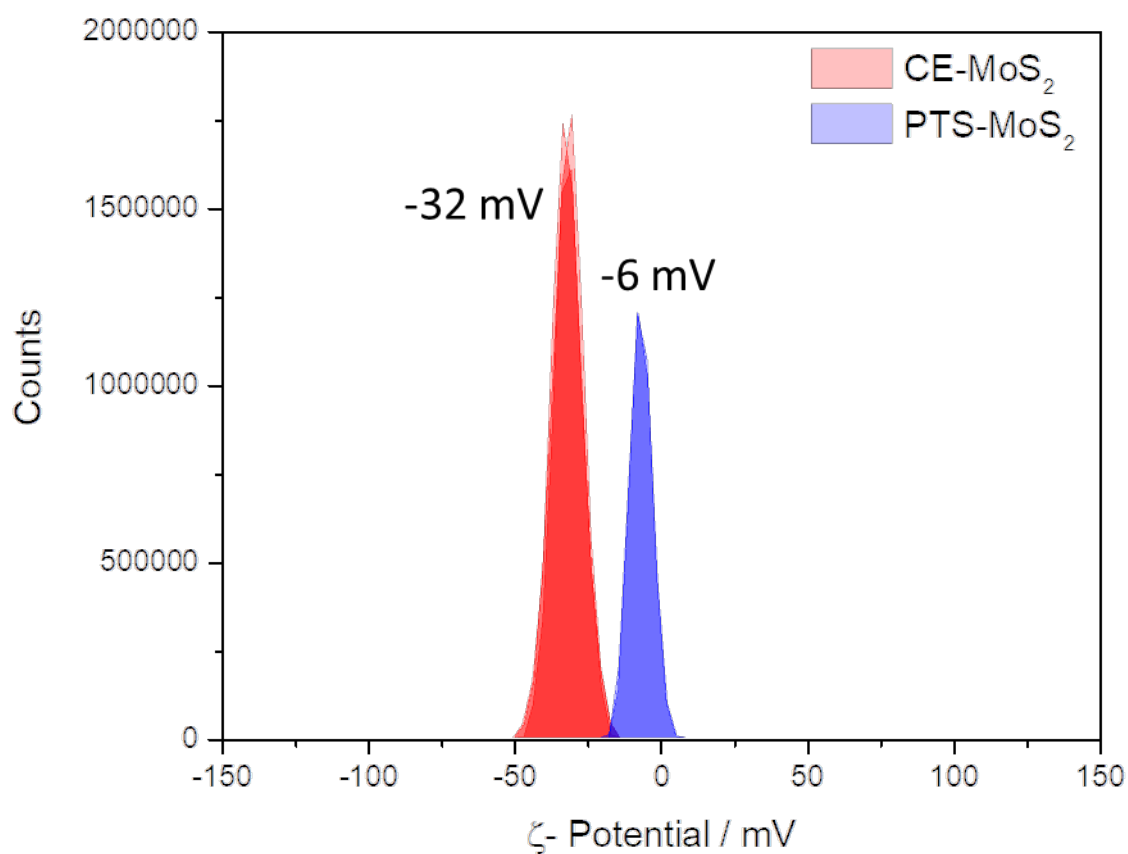

Fig. 1 ξ-potentials of CE-MoS$_2$ and PTS-MoS$_2$. ξ-potentials of CE-MoS$_2$ (red) and PTS-MoS$_2$ (blue) showing the significant decrease of the negative charge on MoS$_2$ surface, after the covalent functionalization.

Thermogravimetric analysis

The degree of functionalization was calculated by comparing the weight loss at 350 °C of the chemically exfoliated MoS_2 and the functionalized one, and assuming that the difference of weight loss between them is only caused for the degradation of the functional groups. As can be seen in Figure 2, the functionalization calculated based on a weight loss is of 30%.
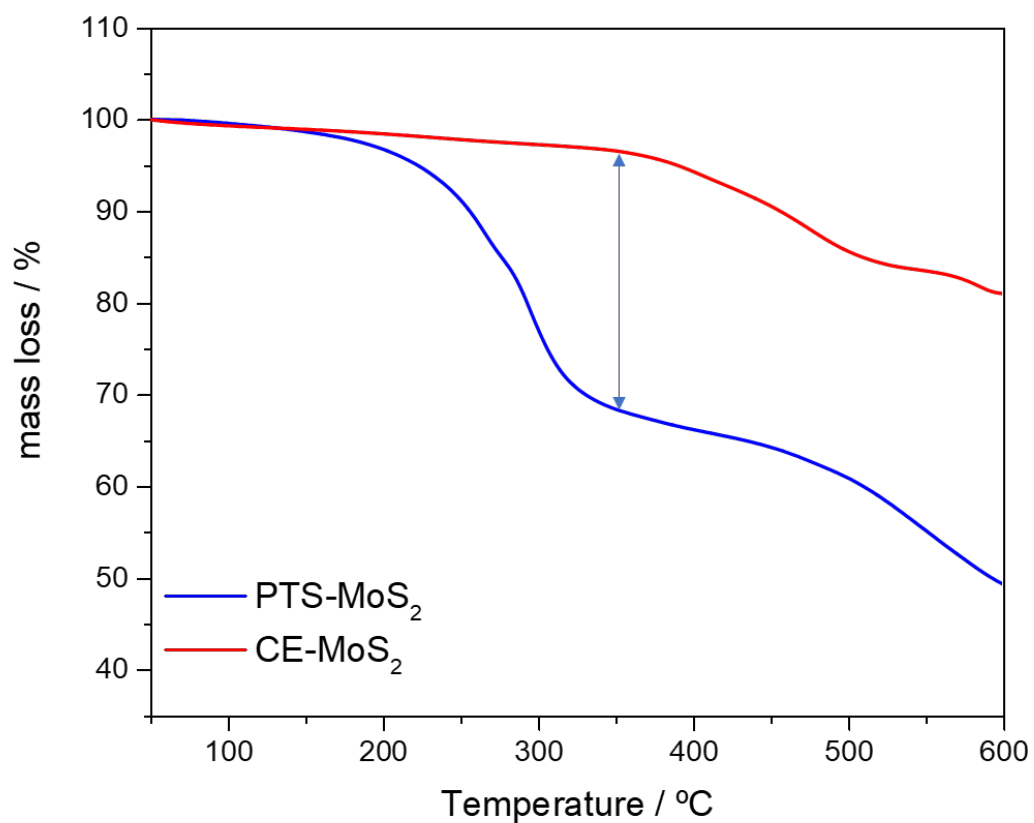

Fig. 2 Thermogravimetric studies. Thermogravimetric analysis under O_2 atmosphere of the CE-MoS_2 (red) and the PTS-MoS_2 (blue). The large mass loss observed in PTS-MoS_2 layers at ~350ºC points out to an effective covalent functionalization of approx. 30%.

Transmission Electron Microscopy

In light of TEM images, CE-MoS$_2$ flakes show their typical lamellar structure (Figure 3a), which is preserved after their functionalization with IPTS (Figure 3b).

The size of the SCO-NPs was determined from TEM (Figure 4) by manual counting using the Image J software. As can be seen in Figure 4, the shape of the SCO-NPs is strongly dependent on the nanoparticles size. This peculiarity is due to the presence of a preferential axial growth, which effect is larger for the biggest nanoparticles.[1,2]
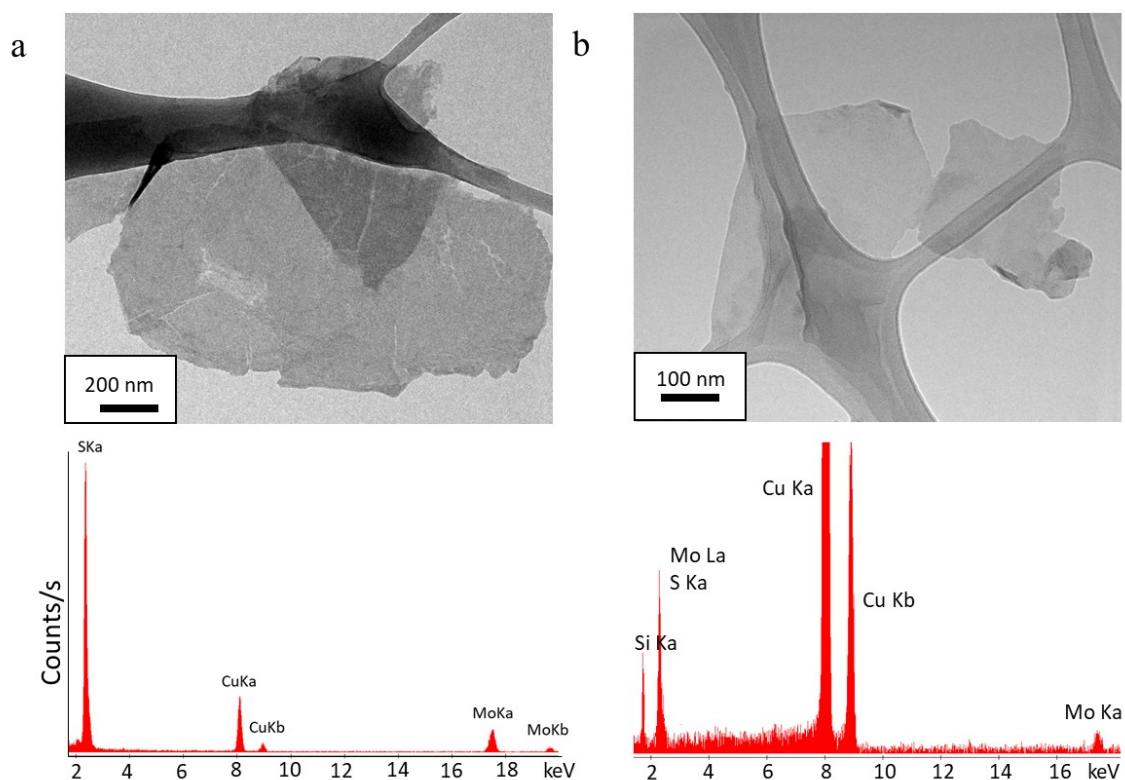

Fig. 3 Transmission electron microscopy EDAX analysis of MoS$_2$. TEM images of CE-MoS$_2$ and PTS-MoS$_2$, (top a and b, respectively) and EDAX of the same systems (bottom). After functionalization with IPTS, MoS$_2$ preserves its 2D nature. The presence of Si and the absence of I supports a covalent functionalization.
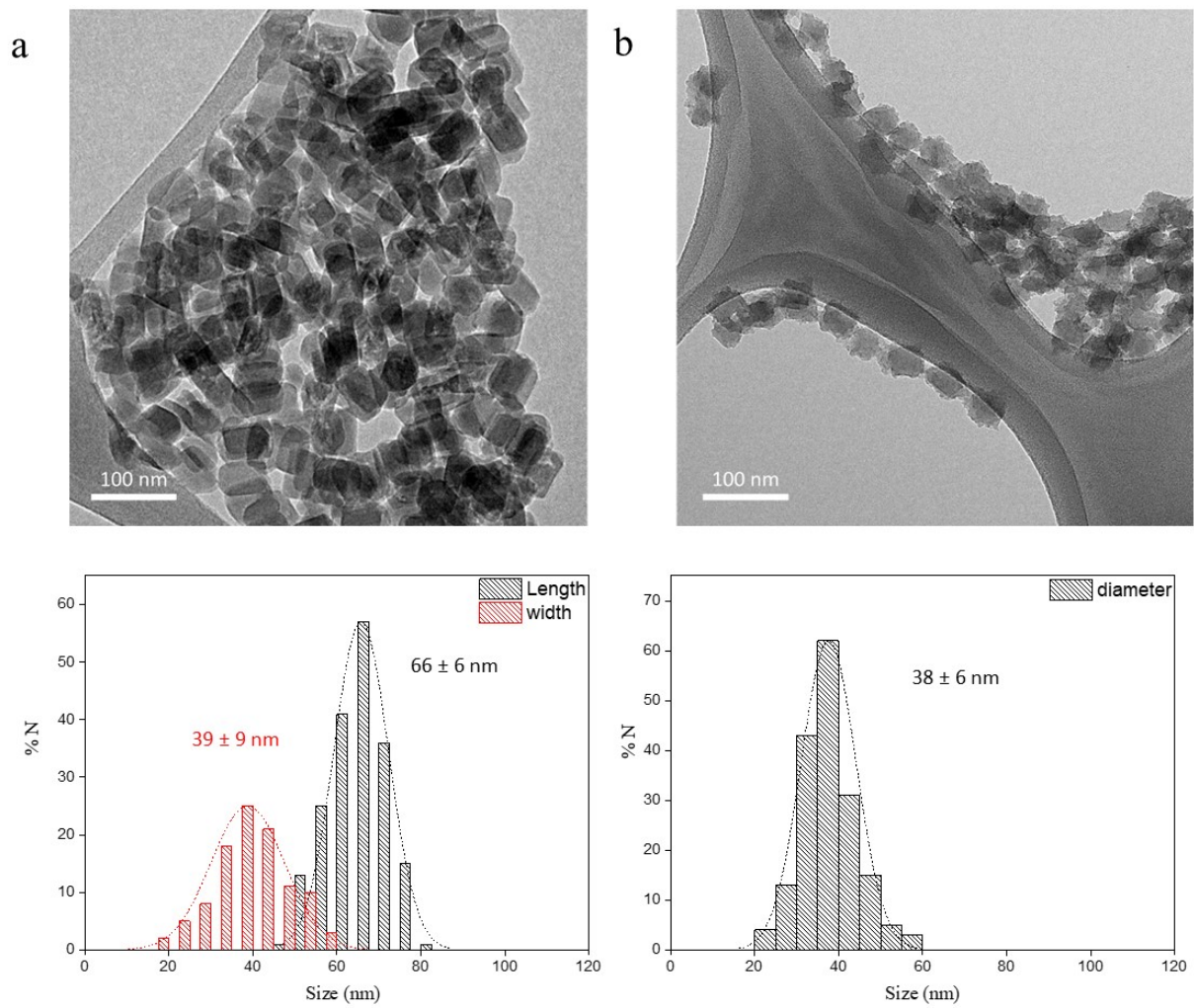
Fig. 4 Transmission electron microscopy of SCO-NPs. TEM images for SCO-NPs 1 (70 nm) and 2 (40 nm), a and b respectively (up). Histograms of the size distributions for the same SCO-NPs developed by manual counting (down).
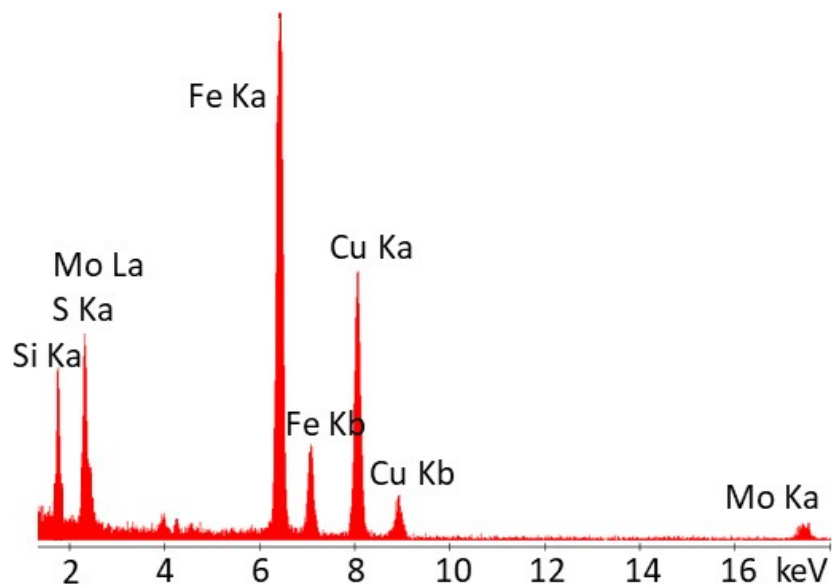
Fig. 5 EDAX study of composite with 40 nm SCO-NPs. EDAX of SCO/MoS$_2$-**2a** shows the presence of Fe and Si (besides Mo and S) after the attachment of the SCO-NPs. Cu contribution comes from TEM grid.

Fig. 6 EDAX study of composite with 70 nm SCO-NPs. EDAX of SCO/MoS$_2$-**1** shows the presence of Fe and Si (besides Mo and S) after the attachment of the SCO-NPs. Cu contribution comes from TEM grid.
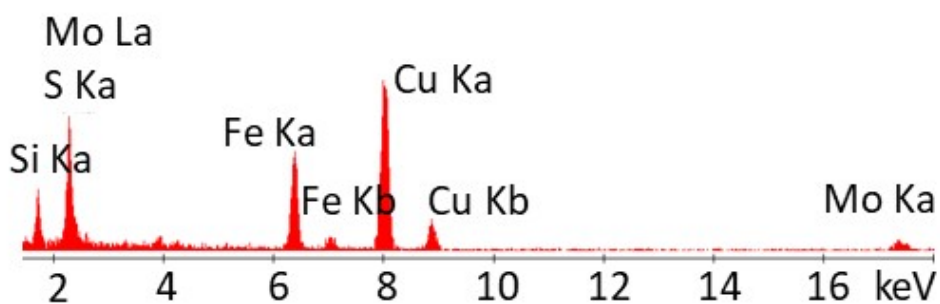
Table 1. *Surface coverage estimations*. *Percentage of SCO surface coverage for the hybrid structures SCO/MoS$_2$.*

	Coverage / %
SCO/MoS$_2$-**1**	78 ± 2
SCO/MoS$_2$-**2a**	82 ± 3
SCO/MoS$_2$-**2b**	50 ± 2
SCO/MoS$_2$-**2c**	100

X-ray Photoemission Spectroscopy

Characteristic bands of Mo^{4+} and S^{2-} of the CE-MoS$_2$, PTS-MoS$_2$, and SCO/MoS$_2$-**1** are observed in Figure 2 (Main text). Two different contributions can be deconvoluted in CE-MoS$_2$, where a predominant contribution corresponds to the 1T phase (~85%), at ~228 eV (*3d$_{5/2}$*) and ~231 eV (*3d$_{3/2}$*) for Mo and ~161 eV (*2p$_{3/2}$*) and ~162 eV (*2p$_{1/2}$*) for S, and the secondary contribution is related to the unaltered original 2H phase, at ~229 eV (*3d$_{5/2}$*) and ~232 eV (*3d$_{3/2}$*) for Mo and ~162 (*2p$_{3/2}$*) and ~163 (*2p$_{1/2}$*) for S. In the case of the PTS-MoS$_2$ and SCO/MoS$_2$ only the contributions of the 2H phase are observed.

Table 2. XPS analysis of CE-MoS$_2$. Summary of the main peaks Mo and S XPS of CE-MoS$_2$. 2H and 1T phases are present.

	Mo*3d$_{5/2}$*	**Mo*3d$_{3/2}$***	**S*2p$_{3/2}$***	**S*2p$_{1/2}$***
MoS$_2$-2H	229.2 eV	232.5 eV	162.2 eV	163.3 eV
MoS$_2$-1T	228.2 eV	231.3 eV	161.0 eV	162.1 eV

Table 3. XPS analysis of PTS-MoS$_2$. *Summary of the main peaks Mo and S XPS of PTS-MoS$_2$. Only 1T phase is detected, and a new contribution from the formation of new covalent bond S-C is present.*

	Mo*3d$_{5/2}$*	**Mo*3d$_{3/2}$***	**S*2p$_{3/2}$***	**S*2p$_{1/2}$***
MoS$_2$-2H	229.1 eV	232.2 eV	161.9 eV	163.2 eV
S-C	-	-	163.0 eV	164.3 eV

In order to evaluate the role played by the target molecule and the functionalization protocol in the final MoS$_2$ phase after its covalent functionalization, CE-MoS$_2$ was functionalized with iodoacetic acid following the protocol reported in this article (COOH-MoS$_2$/1), and that reported in *Nat. Chem. 7, 45-49 (2015)*, (COOH-MoS$_2$/2)

Table 4. XPS analysis of COOH-MoS₂/1. *Summary of the main peaks Mo and S XPS of COOH-MoS₂/1. There is a contribution of 1T and 2H phases plus the presence of new covalent bond S-C and some oxide.*

	Mo3d$_{5/2}$	**Mo3d$_{3/2}$**	**S2p$_{3/2}$**	**S2p$_{1/2}$**
MoS₂-2H	229.5 eV	232.7 eV	162.7 eV	164.1 eV
MoS₂-1T	228.6 eV	231.8 eV	161.4 eV	162.6 eV
MoO₂	230.5 eV	233.5 eV	-	-
S-C	-	-	163.1 eV	164.3 eV

Table 5. XPS analysis of COOH-MoS₂/2. *Summary of the main peaks Mo and S XPS of COOH-MoS₂/2. There is a contribution of 1T and 2H phases plus the presence of new covalent bond S-C and some oxide.*

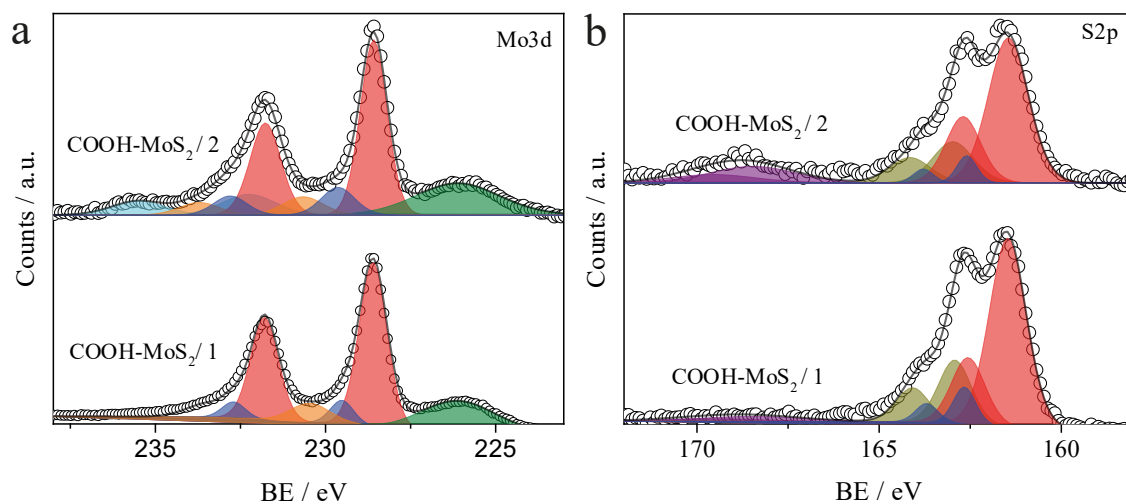|	**Mo3d$_{5/2}$**	**Mo3d$_{3/2}$**	**S2p$_{3/2}$**	**S2p$_{1/2}$**
MoS₂-2H	229.5 eV	232.7 eV	162.7 eV	164.1 eV
MoS₂-1T	228.5 eV	231.6 eV	161.2 eV	162.5 eV
MoO₂	230.5 eV	233.5 eV	-	-
MoO₃	232.5 eV	235.7 eV	-	-
S-C	-	-	163.0 eV	164.2 eV

Fig. 7 XPS analysis of COOH-MoS₂/1 and /2. *Mo 3d (a), and S 2p (b) XPS of the COOH-MoS$_2$/1 and /2. In red the contribution of MoS$_2$-1T, in blue 2H, orange MoO$_2$, cyan blue MoO$_3$, green S2s, dark yellow S-C species and purple SO$_X$. The predominant presence of MoS$_2$ in 1T phase and the formation of a new covalent C-S bond are evidenced.*
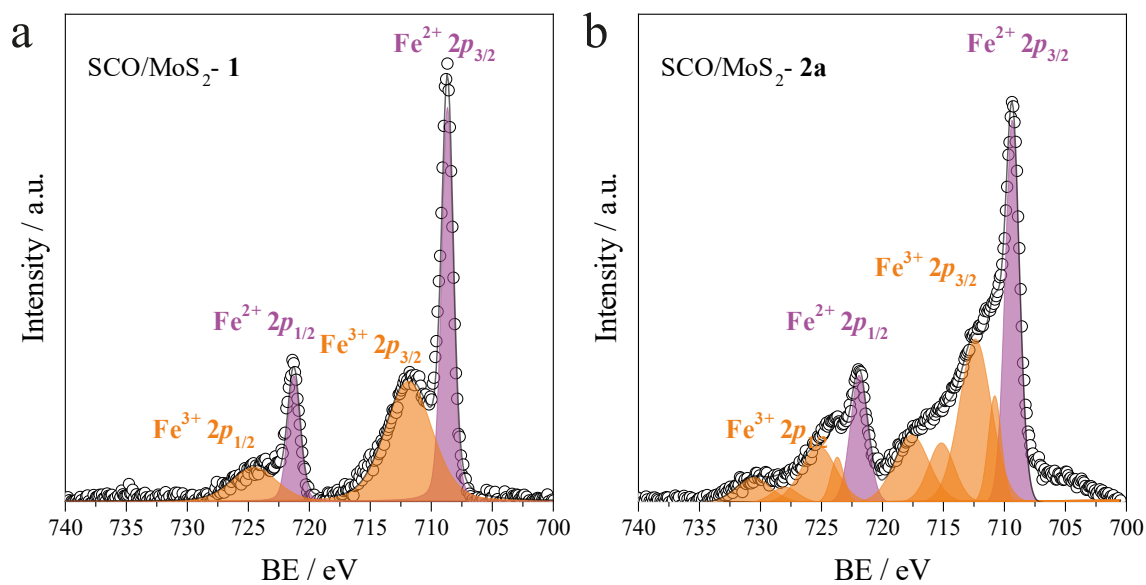

Fig. 8

Fe XPS analysis of composites SCO/MoS₂-1 and 2a. *XPS spectra of Fe 2p for SCO/MoS$_2$-**1** and **2a**, a and b, respectively. The values of the Fe 2p measured by XPS are consistent with a Fe^{2+} in LS state.*
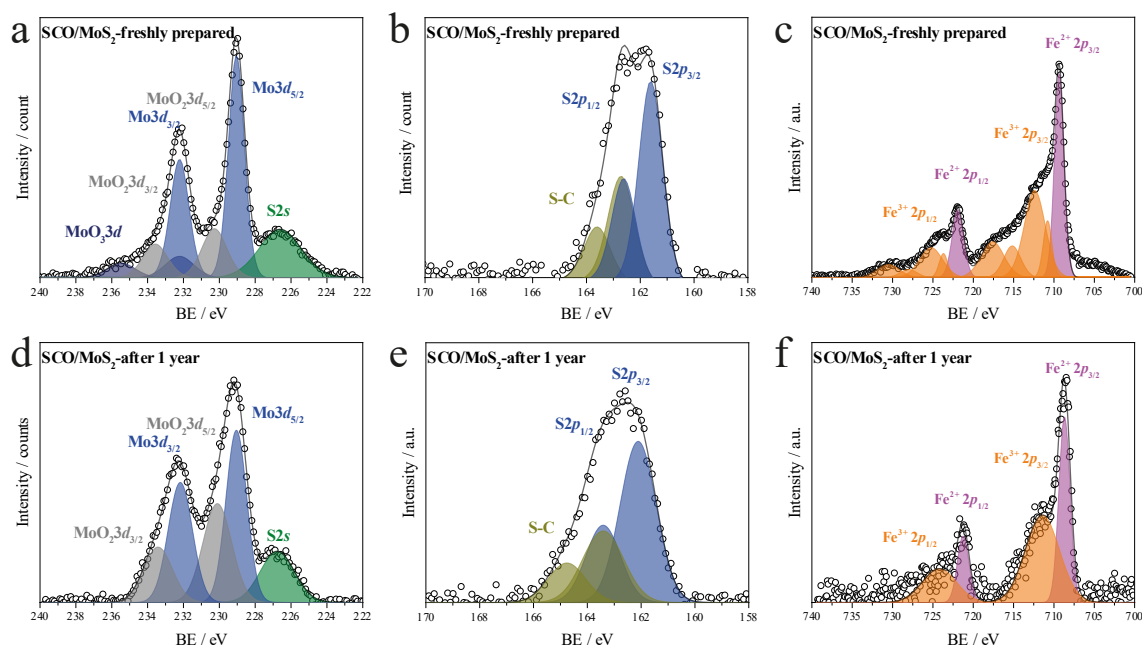
Fig. 9. **XPS study of SCO/MoS₂-2a**. *(a, b, c) Mo3d, S2p and Fe2p XPS spectra of SCO/MoS₂-**2a** freshly prepared. (d, e, f) Mo3d, S2p and Fe2p XPS spectra of SCO/MoS₂-**2a** after 1 year. Contribution of MoS₂ in 2H phase in blue, MoOₓ in grey, S-C species in dark yellow, Fe²⁺in pink and Fe³⁺ in orange. Only a slight oxidation of the system is observed, which supports the robustness of SCO/MoS₂ to aging.*

Magnetic measurements

The elasticity of the silica shell is investigated by the magnetic behaviour of the nanoparticles. To do so, naked nanoparticles of the same SCO coordination compound used in this work have been synthesized. The synthesis of the naked nanoparticles was done by following the same synthetic protocol described in the experimental section for the particles with SiO_2 shell but without adding the silica precursor. Accordingly to the literature, a rigid silica shell would increase the hysteresis width or move the transition temperatures to higher temperatures.[3,4] Nevertheless, in our NPs as Figure 10 shows, the hysteresis remains constant despite de silica shell, indicating their elasticity.
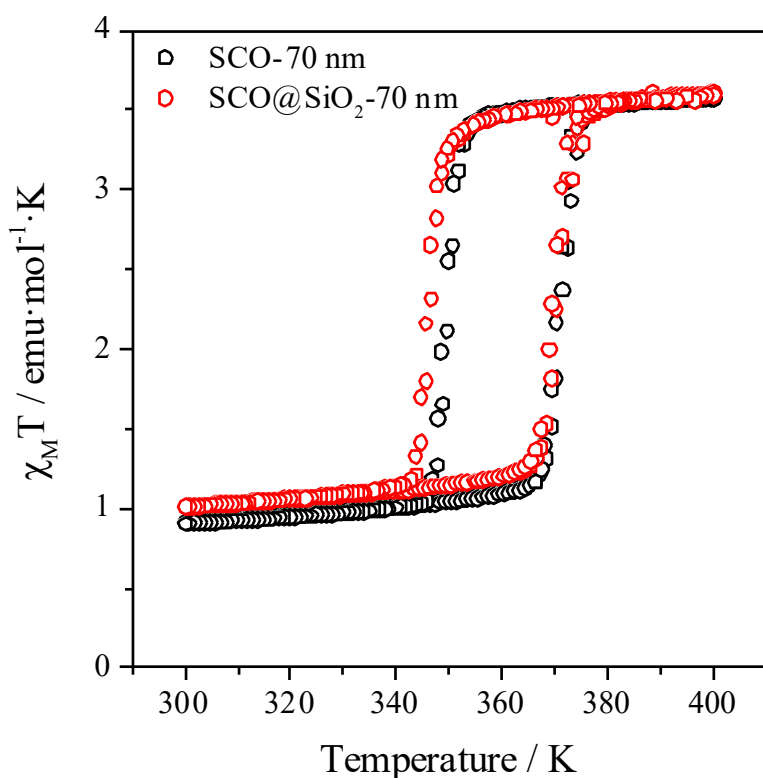

Fig. 10. Bare vs core-shell nanoparticles magnetic properties. *Thermal variation of the $\chi_M T$ product for the bare $Fe(Htrz)_2(trz)(BF_4)$ and core-shell $Fe(Htrz)_2(trz)(BF_4)@SiO_2$ 70 nm SCO-NPs. The almost perfect superposition of both measurements supports the elasticity of the silica shell.*
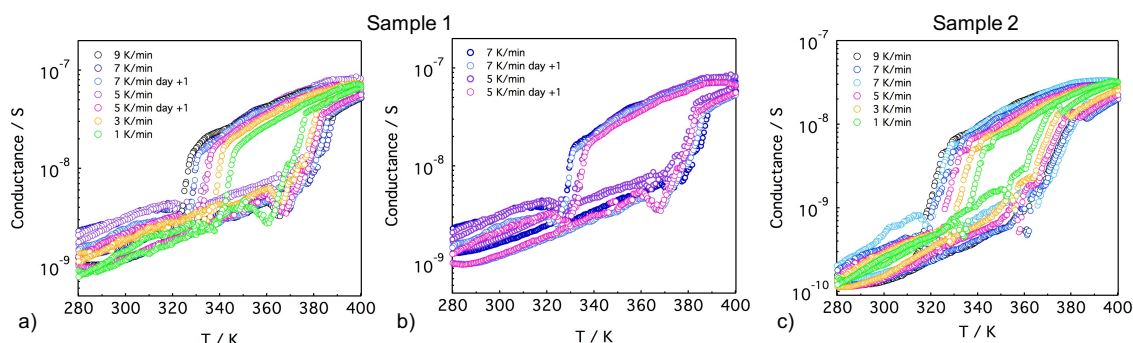
Electrical properties

Samples Stability

Fig. 11*: **Stability of SCO/MoS₂-1 conductance over time**. Conductance vs temperature cycles measured on two different SCO/MoS₂-1 samples demonstrating the robustness of the system. (a) Cycles measured on Sample 1 by applying a bias voltage of 2 V. (b) Detail of Sample 1 measurements on different days. (c) Cycles measured on Sample 2 by applying a bias voltage of 3 V. The width of the hysteresis is scanning rate dependent.*

Figure 11 shows examples of conductance vs temperature cycles performed on two different samples, at different rates and on different days. A broadening in the hysteresis loop as the temperature ramp increases can be observed. This effect is due to the fast temperature scanning rate that leads to a shift between the measured temperature and the real temperature of the sample that has no time to thermalize.

The reproducibility of the measurements over time is demonstrated by the fact that measurements performed at the same scanning rate in different days in not subsequent cycles, well overlap, as shown more in details in Figure 11b. This overlapping proves that switching temperature shift and conductance shift observed over the different cycles are due to thermalization and not to a progressive degradation of the sample.

Reference Samples

In order to provide a proper interpretation of the electrical behaviour displayed by the composite, CE-MoS₂ (in 1T-phase), thermally phase converted CE-MoS₂ (**CE-MoS₂ (2H)**, in 2H-phase), functionalized MoS₂, and bare SCO-NPs were also electrically characterized, Figure 12.

Unfortunately, polimerization at ambient condition of the silane group in the PTS while trying to isolate it, complicates obtaining enough PTS-MoS₂ to compress a pellet and to develop the electrical characterization. For this reason, to properly characterize the electrical behavior of the CE-MoS₂ after its functionalization and consequently 2H phase recovery, an analogous grafting that the one described with the IPTS was carried out but adding a solution 0.1 M of 1-iodooctadecane into the MoS₂ aqueous solution, **C18-MoS₂**.

SCO/MoS$_2$ electrical transport mechanism

In order to explain the observed behavior in our SCO/MoS$_2$ composites, first we wanted to rule out the possibility of an interflake mechanism,[5-7] where volume changes induced by spin transition would be related to the variation of the flake-to-flake distance, improving or hindering the electronic hopping between them. This explanation is rather unlikely because there is a homogeneous distribution of SCO-NPs around the MoS$_2$ flakes, forming a shell around the layers. An increase in volume (LS→HS) will increase then the distance between these layers, decreasing flake to flake contact and, therefore, the overall conductivity, whereas we observe the opposite behaviour. To explore this idea, we prepared a new reference sample formed by the mechanical mixture of SCO-NPs, 70 nm, with CE-MoS$_2$ with the optimum Fe:Mo ratio,~2:1, and its full transport characterization was carried out. However, as expected, only the characteristic transport properties of pure SCO-NPs were observed, as reported in Figure 12c, denoting an interflake mechanism. This result highlights how the mechanism governing SCO/MoS$_2$ composites properties is deeply different and we dubbed it as intraflake, due to the well-known electronic structure modulation of MoS$_2$ layers under strain. In this mechanism, volume change strains the flakes resulting in an intrinsic modulation of the band structure of the layers, and thus its conductivity.[8]
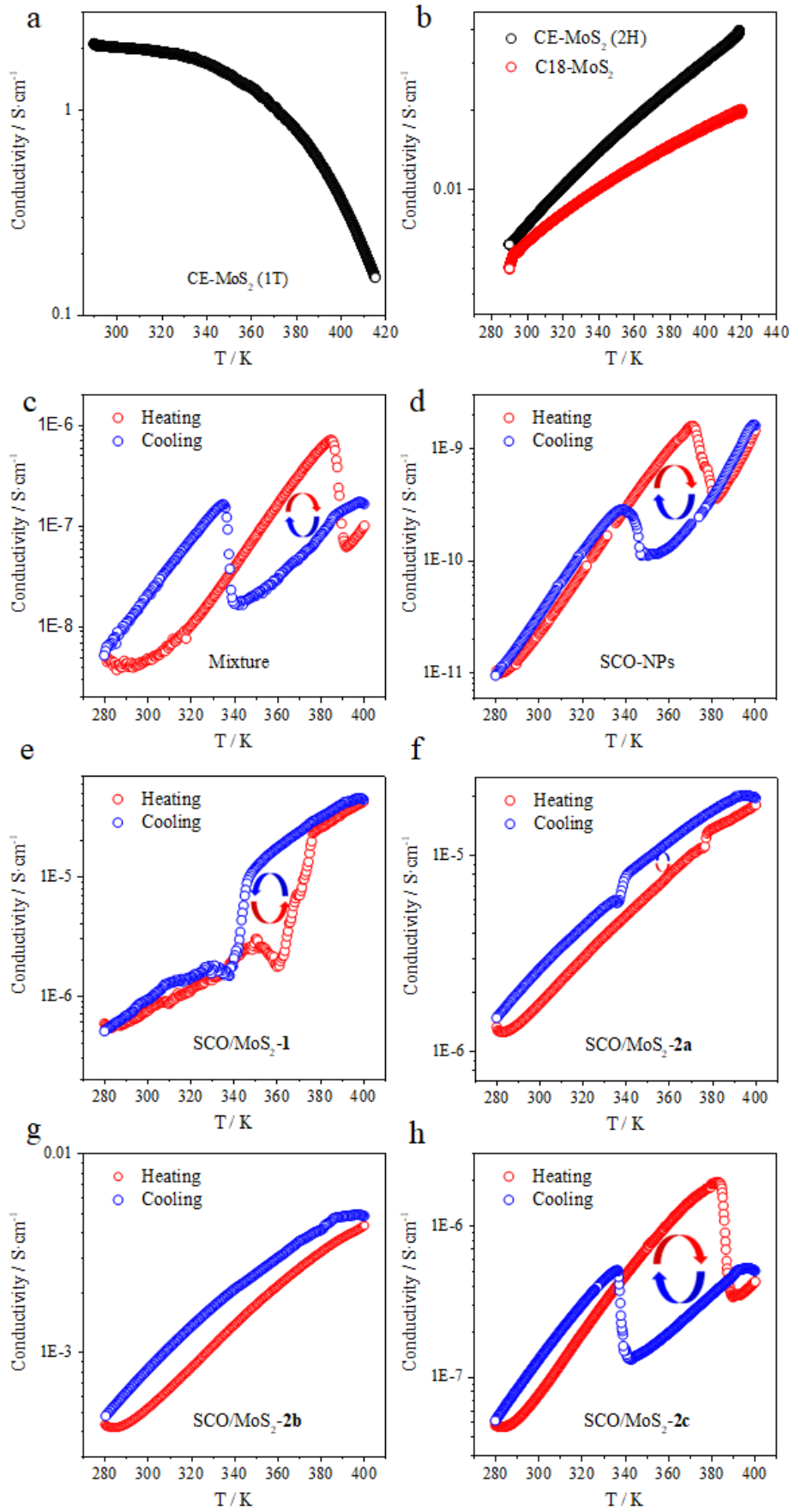
Fig. 12 Transport measurements. Comparison of conductivities as a function of temperature of different samples: (a) CE-MoS$_2$ (1T-phase) and (b) CE-MoS$_2$ (2H) + C18-MoS$_2$; which point out to the semiconducting behaviour of CE-MoS$_2$ after its covalent functionalization. (c) MoS$_2$ mechanically

mixed with SCO-NPs and (d) pure SCO-NPs; which present similar temperature dependence highlighting the importance of chemical bonds between particles and flakes. (e) SCO/MoS$_2$-**1**; (f) SCO/Mo$_2$-**2a**; (g) SCO/Mo$_2$-**2b** and (h) SCO/Mo$_2$-**2c**. These measurements support that when too many SCO-NPs are present, c, the transport dependence with temperature is that characteristic of pure SCO-NPs, while when there are too few SCO-NPs, g, transport dependence with temperature resembles that of pure CE-MoS$_2$ (2H). In optimum ratio the effect on the transport properties is stronger when SCO-NPs are larger, e vs f.

To further investigate the dominating mechanisms in the electronic conductivity modulation of SCO/MoS$_2$ samples, the activation energy (Ea) and pre-exponential factors (σ_o) in both spin-states were extracted from exponential Arrhenius fits of the conductivity vs temperature curves (Figure 13-14). The parameters obtained from the Arrhenius fits for pure SCO-NPs, and SCO/MoS$_2$ composites are given in Table 6-7. For pure SCO-NPs, the Ea and σ_o are both higher in the LS state compared to the HS state, which is in good agreement with the literature (Figure 13 and Table 6).[9] In the case of SCO/MoS$_2$-**1,** the tendency reverses, and the Ea and σ_o in the LS decreases respect to the bare SCO-NPs (Figure 13), getting closer to the values of CE-MoS$_2$ in semiconducting 2H-phase, CE-MoS$_2$ (2H), and C18-MoS$_2$ samples (Figure 14). In sample SCO/MoS$_2$-**2a**, where spin state effect is less intense, Ea and σ_o at low and high spin are similar but closer to that of MoS$_2$ flakes like in SCO/MoS$_2$-**1**. This supports our hypothesis of the current mainly flowing through the MoS$_2$.
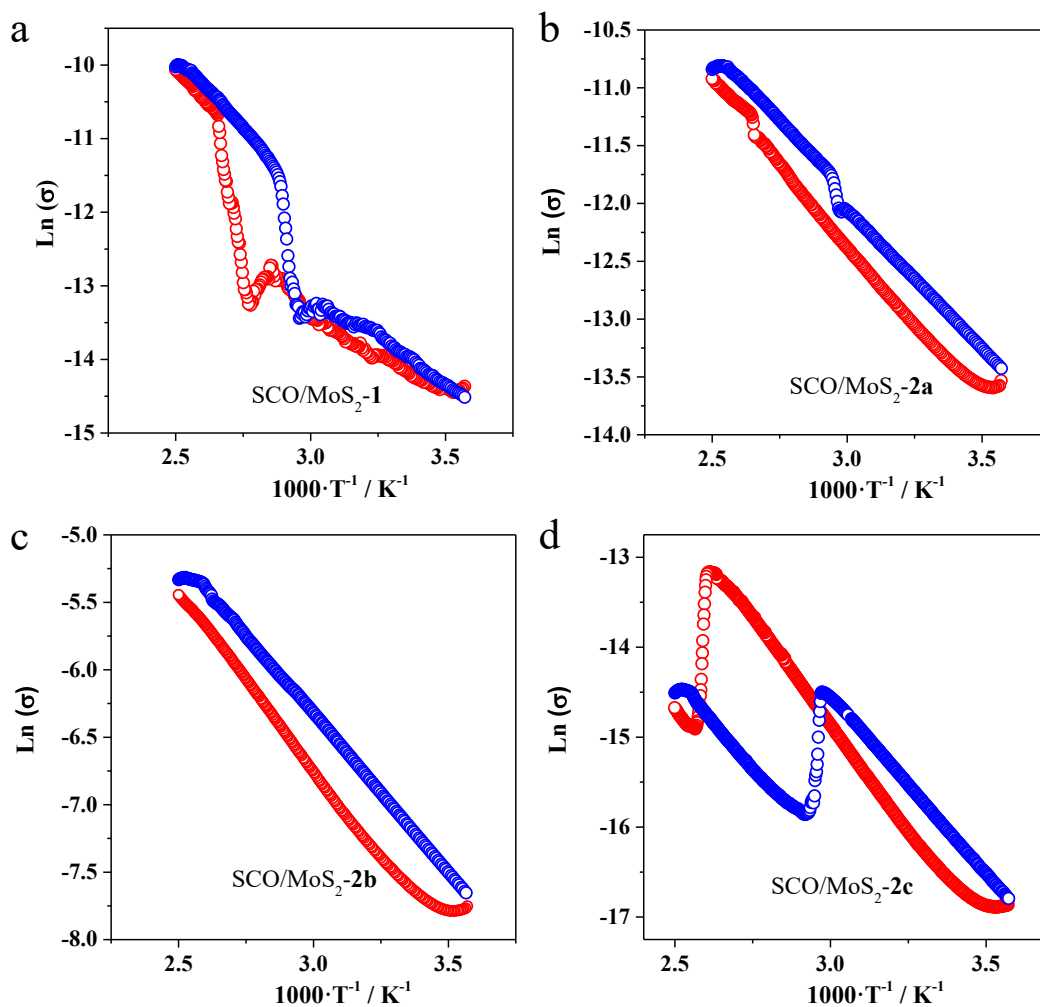
Fig. 13 Arrhenius plots. Arrhenius plot of the logarithm of the conductance versus the inverse temperature of SCO/MoS$_2$-**1**, **2a**, **2b** and **2c** (a, b, c, and d respectively). These plots are used to extract data presented in table 6.
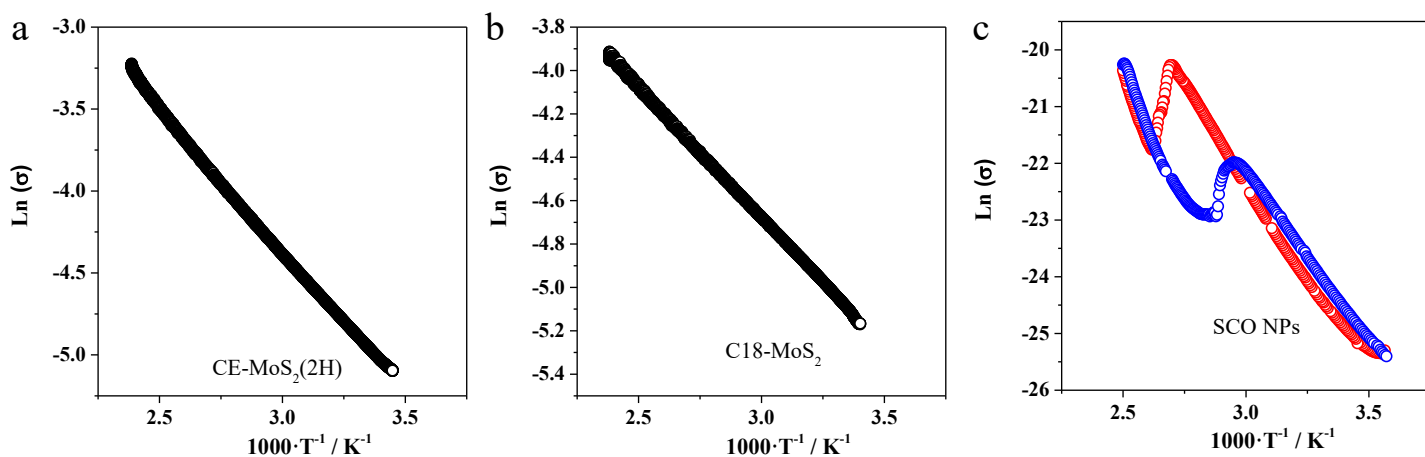

Fig. 14 Arrhenius plots. Arrhenius plot of the logarithm of the conductance versus the inverse temperature of CE-MoS$_2$ (2H) (a), C18-MoS$_2$ (b), bare SCO-NPs (c). These plots are used to extract data presented in table 6 and 7.

Table 6 Summary of SCO-NPs and SCO/MoS$_2$ composites composition and their main electrical properties

	Ea^{LS} / eV	Ea^{HS} / eV	σ_o^{LS} / S·cm^{-1}	σ_o^{HS} / S·cm^{-1}	σ / S·cm^{-1} 300K	$\Delta R \cdot R_0^{-1}$
SCO NPs	0.6	0.5	0.7	6·10^{-04}	2·10^{-11}	-
SCO/MoS$_2$-**1**	0.2	0.4	2·10^{-03}	2	1·10^{-06}	-0.9±0.2
SCO/MoS$_2$-**2a**	0.2	0.2	2·10^{-02}	1·10^{-02}	2·10^{-06}	-0.3±0.02
SCO/MoS$_2$-**2b**	0.2	-	0.2	-	1·10^{-03}	-
SCO/MoS$_2$-**2c**	0.4	0.2	0.6	6·10^{-04}	7·10^{-08}	-

Table 7. *Summary of annealed CE-MoS$_2$ and functionalized C18-MoS$_2$ electrical properties.*

	Ea / eV	σ_o / S·cm^{-1}	σ / S·cm^{-1} 300K
Annealed CE-MoS$_2$	0.2	2	8·10^{-03}
C18-MoS$_2$	0.1	0.3	6·10^{-03}

Gauche factor

Finally, we can estimate the piezoresistive properties of the SCO/MoS$_2$-**1** hybrid by using the previous results in conductivity (Table 6), and PL measurements. These are accounted by the Gauge factor, $G = \dfrac{\Delta R}{\varepsilon \cdot R_0}$, where ε is the applied strain, estimated from the PL shift inside the hysteresis (~0.6%), R$_0$ is the resistance of the non-strained material and ΔR the resistance changes inside the hysteresis, obtained from the electrical measurements (Table 6). Thus, a negative *G*-value has been calculated (G ≈ -150 which falls within the range of values reported for MoS$_2$ monolayers, being clearly below those characteristic for multilayers, G ≈ -40)[10] and proving that the piezoresistive properties of ultrathin MoS$_2$ layers remain in the heterostructure.
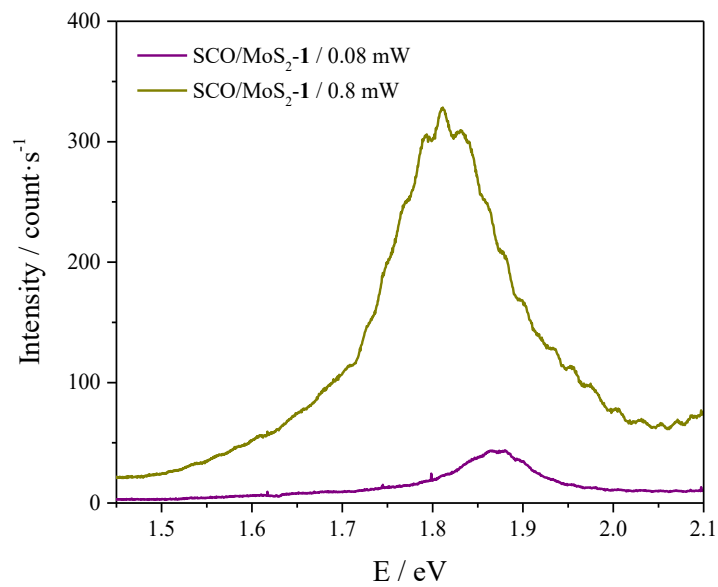
Optical properties

Fig. 15. ***Untreated PL spectra.*** *No normalized PL of SCO/MoS₂-**1** at 0.08 mW (purple plot) and 0.8 mW (yellow plot) of excitation power showing the higher intensity expected when higher excitation power is used.*

References:

1. Urakawa, A. *et al.* Combined, modulation enhanced X-ray powder diffraction and raman spectroscopic study of structural transitions in the spin crossover material [Fe(Htrz)$_2$(trz)](BF$_4$). *J. Phys. Chem. C* **115,** 1323–1329 (2011).
2. Grosjean, A. *et al.* Crystal structures and spin crossover in the polymeric material [Fe(Htrz)$_2$(trz)](BF$_4$) including coherent-domain size reduction effects. *Eur. J. Inorg. Chem.* 796–802 (2013). doi:10.1002/ejic.201201121
3. Herrera, J. M. *et al.* Studies on bifunctional Fe(II)-triazole spin crossover nanoparticles: Time-dependent luminescence, surface grafting and the effect of a silica shell and hydrostatic pressure on the magnetic properties. *J. Mater. Chem. C* **3,** 7819–7829 (2015).
4. Raza, Y. *et al.* Matrix-dependent cooperativity in spin crossover Fe(pyrazine)Pt(CN)$_4$ nanoparticles. *Chem. Commun.* **47,** 11501–11503 (2011).
5. Koo, Y.-S. & Galán-Mascarós, J. R. Spin Crossover Probes Confer Multistability to Organic Conducting Polymers. *Adv Mater* **26,** 6785–6789 (2014).
6. Chen, Y.-C., Meng, Y., Ni, Z.-P. & Tong, M.-L. Synergistic electrical bistability in a conductive spin crossover heterostructure. *J. Mater. Chem. C* **3,** 945–949 (2015).
7. Rat, S. *et al.* Coupling Mechanical and Electrical Properties in Spin Crossover Polymer Composites. *Adv Mater* **30,** 1705275–6 (2018).
8. Biccai, S. *et al.* Negative Gauge Factor Piezoresistive Composites Based on Polymers Filled with MoS$_2$ Nanosheets. *ACS Nano* **13,** 6845–6855 (2019).
9. Holovchenko, A. *et al.* Near Room-Temperature Memory Devices Based on Hybrid Spin-Crossover@SiO$_2$ Nanoparticles Coupled to Single-Layer Graphene Nanoelectrodes. *Adv Mater* **28,** 7228–7233 (2016).
10. Manzeli, S., Allain, A., Ghadimi, A. & Kis, A. Piezoresistivity and Strain-induced Band Gap Tuning in Atomically Thin MoS$_2$. *Nano Lett.* **15,** 5330–5335 (2015).